A New Toolbox for Experiments with Ultracold ^{6}Li

Diplomarbeit in Physik

zur Erlangung des akademischen Grades
eines Magisters der Naturwissenschaften
vorgelegt von

Christoph Kohstall

durchgeführt am Institut für Experimentalphysik
der Fakultät für Mathematik, Informatik und Physik
der Leopold-Franzens-Universität Innsbruck
unter der Leitung von
Univ.-Prof. Dr. Rudolf Grimm

Innsbruck, Februar 2007

Zusammenfassung

Die aktuelle Zielsetzung unseres Experiments ist die Erforschung des Übergangs von einem Bose-Einstein Kondensat (BEC) zu einem superfluiden Bardeen-Cooper-Schrieffer (BCS) Zustand. Hierzu präparieren wir ein ultrakaltes Gas fermionischer ^{6}Li Atome in einer optischen Dipolfalle, die durch einen fokussierten Laserstrahl erzeugt wird. Eine breite Feshbach-Resonanz bei 834 G erlaubt uns eine gezielte Variation der Wechselwirkung zwischen den Atomen durch Anlegen eines Magnetfeldes. Absorptionsbilder geben Aufschluss über die Dichteverteilung der Atomwolke. Mit Hilfe dieses experimentellen Aufbaus können wir verschiedene Wechselwirkungsbereiche dieses atomaren fermionischen Vielteichchen-Systems untersuchen.

In dieser Arbeit stellen wir zwei Aufbauten vor, die die Möglichkeiten zur Manipulation und Detektion erweitern:

- Eine optische Dipolfalle, deren Position und Form gesteuert werden kann: Hierzu entwickeln und konstruieren wir ein System zur Ablenkung des Laserstrahls. Eine langsame Ablenkung führt zu einer einfachen Verschiebung der Falle, da die Atome adiabatisch folgen. Wird die Ablenkung sehr schnell moduliert, ist für die Bewegung der Atome nur noch ein gemitteltes Fallenpotential verantwortlich, was einer Änderung der Form entspricht.

- Ein hochauflösendes Abbildungssystem, das die optischen Grenzflächen der Vakuumapparatur berücksichtigt: Befindet sich zwischen Objekt und Linse des Abbildungssystems eine Glasplatte, kommt es zu optischen Aberrationen, besonders dann, wenn die optische Achse nicht senkrecht auf der Glasplatte steht. Wir zeigen, wie diese Aberrationen korrigiert werden können.

Obwohl diese Aufbauten an unser ^{6}Li-Experiment angepasst sind, können sie leicht auf andere Experimente zur Erforschung kalter Gase übertragen werden.

Derzeit setzen wir die entwickelten Systeme zur Anregung und Messung kollektiver Oszillationen ein und viele weitere Experimente werden dadurch möglich.

Abstract

Our field of research is the crossover from a Bose-Einstein condensate (BEC) to a Bardeen-Cooper-Schrieffer (BCS) superfluid. A gas of fermionic ^{6}Li atoms is cooled to ultra-low temperatures in an ultra-high vacuum environment. It is confined in an optical dipole trap formed by a single focused laser beam. The two-body interaction is controlled by means of a Feshbach resonance. Absorption imaging reveals the density distribution of the atom cloud. This experimental setup allows to investigate different interaction regimes of an ensemble of fermionic atoms.

This thesis reports on two technical upgrades of the control and detection of the atomic sample:

- An optical dipole trap that can be moved and deformed in a versatile and well-controlled way: The design and implementation of a scanning system, which deflects the single focused laser beam, is discussed. A slow deflection represents a displacement of the trap because the atoms follow adiabatically. For rapidly modulated deflection, the atoms just respond to the average laser beam intensity; the trap is effectively deformed.

- A high-resolution imaging system that is optimized for imaging through a window of a vacuum chamber: The window induces aberrations to the diverging imaging light especially if the window is not perpendicular to the imaging axis. We report on the correction of those aberrations to gain high resolving power.

These upgrades were developed for the ^{6}Li apparatus but can be easily adapted to other cold-atom experiments.

The new scanning and imaging systems are currently employed to excite and measure collective oscillations of the atom cloud and open up the way to many more exciting novel experiments.

Contents

Contents

1. Introduction

Knowledge in physics has been growing for many centuries. Throughout this progression, a variety of procedures and methods has been developed. Let us pick three of those which have proven to be extremely powerful in extending our physical understanding.

- A system of interest is *isolated*. Then it is not perturbed by influences from the outside, hence allowing a clear view on the system. That is what Einstein did when he developed the theory of special relativity. In his gedanken experiments, he isolated a system of fast moving objects from the field of gravity. After having described this system, he could move on to account for gravity yielding an even more advanced theory: The theory of general relativity.
- The dependence of the system on different *parameters* is investigated. Those dependencies yield physical laws. Following this procedure, Galileo Galilei could find a law for acceleration through gravity. He varied the time of acceleration and the mass of the object to find that the final velocity is proportional to the time and independent of the mass. In contrast to the general belief that he performed those experiments on the tower of Pisa, he used balls rolling down an inclined plane.
- The *response* of the system to influences from outside is investigated in order to explore physical properties. We test if an object is solid by touching it or see its color when light shines onto it. Scientific methods can be much more sophisticated but are of the same kind.

From physics in general we move to the branch of physics we are working in: Ultracold gases of fermionic atoms. With such a system we are advancing the understanding of very basic states of matter, as the building blocks of all matter are fermions. All the methods mentioned above are applied to ultracold Fermi gases.

- A system of ultracold fermions is *isolated* in many ways. It is prepared and stored in vacuum, thus isolated from other particles which could destroy it. Gravity is compensated by levitation. The sample is isolated from other constituents since only one species of atoms in well defined internal quantum states is trapped.

- The ability to control different *parameters* is one of the greatest benefits of ultracold atomic systems. Cooling methods, which were developed throughout the progress of ultracold physics, provide the control of temperature. We have also learned how to tune the interaction strength between the particles. Temperature and interaction strength are crucial parameters for the onset of phase transitions that are not yet fully understood.

- Any experiment probes the *response* of the cloud to a stimulus from outside in order to reveal the properties of the cloud. One example is to record the loss of atoms depending on the frequency of incident radio frequency radiation in order to learn about different energy scales. Another example is to excite oscillation modes which are used to indicate phase transitions.

In other systems of interacting fermions, it is often not possible to isolate the system, to change the parameters or to investigate a response to a stimulus. Thus, ultracold Fermi gases promise to foster a better understanding of those systems, e.g. high temperature superconductors and neutron stars.

The focus of this thesis is the design of a scanning system which generates an atom trap of which shape and position can be changed. Such a trap comes along with possibilities that add to the last two methods from above as follows:

- The ability to change the trap adds controllable *parameters*: The strength of the confinement and the form of the potential, which can - among others - be quadratic, quartic or box-like.

- A change in trapping potential represents a stimulus to the atom cloud. One well-known example is taking time-of-flight images. After a certain time, the *response* of the cloud to switching off the trap is imaged. This trivial change in trapping potential can be upgraded with the scanning system by letting the expansion start from different trap shapes. The ability to change position or shape of the trap in time allows a whole range of experiments. One example is to excite oscillation modes that can be used to probe various properties of the atom cloud.

By now, we have extensively used the scanning system to excite modes in the atom cloud and will continue to exploit the dependence on trapping parameters to investigate ultracold fermionic gases.

The thesis is structured as follows. We start with three guides to the experiment on three different degrees of difficulty. We illustrate some basic principles for the reader who is just interested, we sketch some of the underlying physics for the reader who has some background in physics, and we give detailed information on our experiment to the reader who is specialized in atomic physics (chapter 2). After a brief résumé of experiments performed with our machine, we list a variety of future experiments that motivate the construction of two new setups (chapter 3). We then describe the design, implementation and performance of those upgrades (chapter 4). The scanning system, one of these setups, enables us to create various trapping potentials that will be used for different experiments (chapter 5). By the time of writing this thesis, some of these experiments have already been performed. But since this thesis focuses on the technical part of the experiments, the results can be found in our recent publications. We close by listing experiments to be performed in the future (chapter 6).

2. Hitchhiker's Guide to the Experiment

Choosing a guide

This chapter streaks highlights of the technology, the experimental procedure and the scientific benefit of our experiment (Fig. 2.1). Every reader, no matter which level, should find an appropriate column and should feel free to jump to the right column for more details on a subject or to the left for a simpler approach:

Just interested	**Physics major**	**Atomic physicist**
We pick out a few neat concepts and explain them in a figurative way.	We sketch of the underlying physics of our experiment.	We focus on special features of our ^{6}Li BEC-BCS crossover experiment.

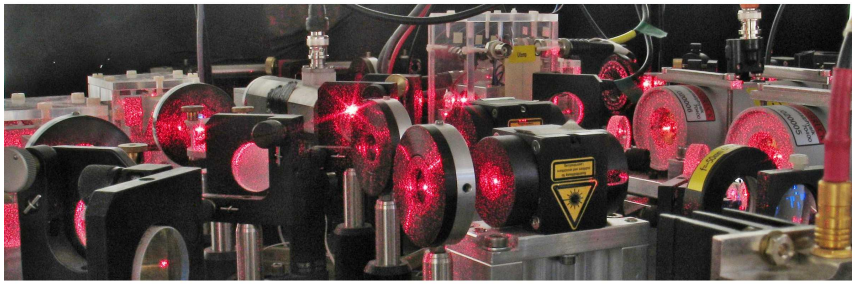

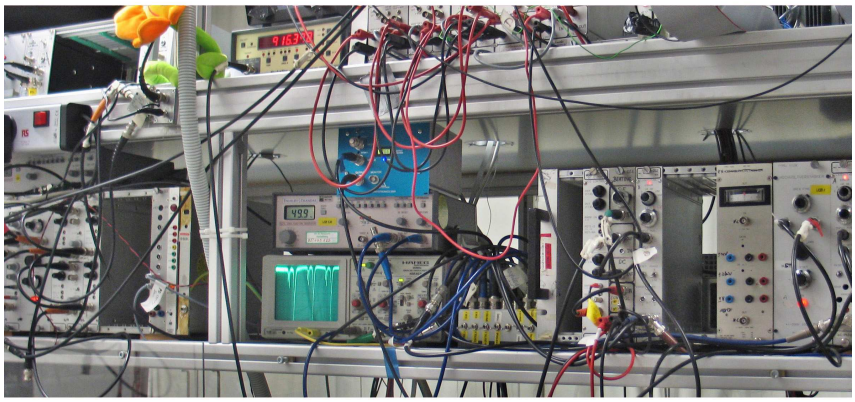

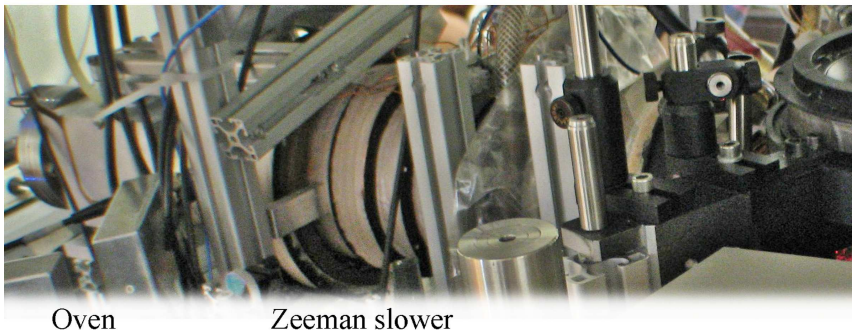

Oven Zeeman slower

Figure 2.1.:
Part of the laser system. The scattered light you see has a wavelength of about 671 nm and is resonant with ^{6}Li moving towards it.
Part of the electronics. Most of the devices on this picture are for the current, temperature and cavity length control of the diode lasers.
Part of the vacuum chamber. The oven is inside the aluminum cube on the left. One can see some coils of the Zeeman slower. The gas is trapped in the glass cell where all the red light is scattered.

Ultracold physics

The last letter of BEC stands for condensation. It reminds of the condensation from water vapor to water. Both types of condensation are induced by cooling. To reach BEC, we have to make the atoms colder than anything else in the universe. Thus, the technical challenge of the experiment is cooling which means slowing down the atoms. When water vapor condenses, particles pile up next to each other. When a BEC forms, all particles merge to "one". What means "one"? Only quantum mechanics can treat this phenomenon properly. Here, we just want to share the fascination of such an object: A "super particle" is formed. The constituent particles lose their individuality. Millions of atoms behave like one and the same. Quantum mechanics becomes visible.

The field of ultracold physics is entered when the motional degrees of freedom in a gas no longer obey the Boltzmann statistics. The Bose-Einstein and Fermi-Dirac statistics take over to describe the two fundamentally different classes of particles: bosons and fermions. For bosons below a critical temperature, the Bose-Einstein statistics predict a phase transition to a superfluid, the Bose-Einstein condensate (BEC). Fermions fill a so-called Fermi sea at very low temperature. For weak attraction, the BCS (Bardeen Cooper Schrieffer) theory predicts a phase transition to a superfluid of weakly coupled fermions. But fermions can also strongly couple and form dimers which are bosonic and condense to a BEC. The transition between these regimes is called BEC-BCS crossover.

The ability to tune the scattering length a between atoms by means of a Feshbach resonance is a unique tool in ultracold physics that we use to explore different interaction and coupling regimes among fermions. Starting with negative a in our experiment, the Fermi gas is in the collisionless regime where collisions are Pauli blocked. An increase of a leads into the collisional regime. Then the critical temperature for the Cooper instability is ramped up and the strongly interacting BCS regime is accessed. For large a, the unitarity regime is accessed. Here, a diverges and changes sign. For positive a, the fermions occupy a weakly bound molecular state. Those strongly coupled pairs are bosonic and condense to a strongly interacting BEC. This transition is known as the BEC-BCS crossover.

2.1. Technology

Vacuum

To keep coffee hot you use a thermos flask. The vacuum in such a bottle prevents the transfer of heat. To keep the atoms cold we also use vacuum - one that is a billion times better.

A BEC is one of the most fragile objects known to man. A few collisions with thermal atoms would destroy it. For preparation and storage the pressure has to be about 10^{-10} mbar.

The vacuum chamber is divided into two sections with differential pumping in between. The oven is at $\approx 10^{-8}$ mbar and the pressure in the science chamber is below 10^{-10} mbar.

Lasers

We manipulate the atoms with light. To do this, we have to choose exactly the right color of light. Think of a color palette with fifty million different colors, ranging from red to blue. Only one of these colors interacts with the atoms. That is how precisely we have to adjust the frequency of the lasers. We also use lasers for trapping the atoms. To do this, we need 1000 times more laser beam power than would be enough to burn your eye.

The tremendous progress in atomic physics in the last decades is ascribed to the fact that physicists have learned to manipulate the internal and external degrees of freedom of atoms with light. We use diode lasers where the exact transition frequency and detuning is adjusted with an external cavity. A master laser, that serves as reference for all other lasers, is locked to a certain transition of a different isotope, ^{7}Li.

The transition frequencies of ^{6}Li are derived from a master laser that is locked to a crossover line of ^{7}Li in a vapor cell. A slave laser is detuned via beat lock close to the $2S_{1/2}$ to $2P_{3/2}$ line of ^{6}Li. The light is split and the exact frequencies for cooler, repumper and Zeeman slower beam are adjusted with AOMs. These beams are used to injection lock four laser diodes, that amplify the beams to $\approx$ 20 mW each.

Control

One measurement takes about 20 sec. In this period of time hundreds of events take place to prepare, stimulate and probe the atomic sample: laser beams are tuned and ramped in intensity, fields are switched, signals are read out and images are taken. All those steps are computer controlled.

Every run of the experiment is a series of many accurately timed events. Besides digital switching, ramps have to be driven. The step size in time is given by the duration of one cycle of output (5 μs) and the step size in voltage is given by the digital to analog converter (20 V/2^{16}).

For computer control, we use an Adwin Gold with internal processor that is programmed via Ethernet. It drives two analog and one digital expanders. The user interface is programmed in Labview which communicates with the Basic program of the Adwin.

2.2. Experiment

Oven

For the experiment we need a gas of lithium, the lightest metal. Although lithium is solid, some atoms escape from its surface. That is also the reason why you can smell metals. By the way: Salt o lithium is used for treating elation or mania.

Heating a rod of metallic ^{6}Li to 340°C provides an atomic beam. Since the lithium is embedded in a copper tube the temperature has to stay below 400°C. At higher temperature the components start to form an alloy.

An oven provides a beam of ^{6}Li atoms. Only a small fraction of the beam is slowed. Most of it is dumped on the window where the Zeeman slower beam enters the vacuum chamber. The window is heated to avoid coating with lithium.

Zeeman slower

Coming out of the oven the atoms are very fast; about the speed of sound. The Zeeman slower reduces their velocity - with light. According to Einstein one can think of light as particles. Those particles are much lighter than the atoms, but shooting many of them against an atom slows it down. In this simple image all the details of the light-atom interaction were neglected. We will learn more about that later.

A Zeeman slower decelerates the atoms coming out of the oven by the light pressure of a counter propagating beam. As the light frequency in the reference frame of the atom changes with velocity due to the doppler effect, the light is kept on resonance by adjusting the transition frequency with a magnetic field. A certain velocity class is decelerated all along the Zeeman slower. Slower atoms are decelerated at the end and faster ones are lost.

The Zeeman slower is the first cooling stage. Since the scattering along the tube is a stochastic process, atoms might get out of resonance. Frequency modulation of the slowing beam broadens the range where the resonance condition is fulfilled. The Zeeman slower beam drives a closed transition and no repumper is needed; but to improve the capture performance of the MOT an additional repumper beam is added to the Zeeman slower beam.

MOT

The "MOT" traps the atoms and cools them further. Say you, representing the atom, are swimming in a lake with waves, representing the light. You swallow water when the waves hit you with a certain frequency. Whenever you swallow, you slow down. The frequency of the waves is below this critical frequency. When you swim towards the waves, they hit you more often - this is called the Doppler effect. Then you swallow and slow down. If those waves come from all sides you couldn't swim in any direction. You would be slowed down. That is the principal of cooling atoms with light. To understand why this cooling mechanism is limited, we come back to the particle picture of light: an atom can't get slower than the velocity it gets from a single kick.

The atoms decelerated by the Zeeman slower are captured in a magneto-optical trap (MOT). The atom cloud in there is often referred to as optical molasses because the atoms experience a velocity dependent friction in the light field. Slightly red detuned light comes from all directions. Due to the Doppler shift, the light is predominantly resonant with atoms moving towards it. This slows the atom down because the subsequent spontaneous emission is random. The confinement in real space is achieved with a magnetic field minimum. The field lifts the degeneracy of the atomic m-levels corresponding to σ_+ and σ_- transitions. The laser configuration is chosen such that atoms on a specific side of the field minimum are closer to resonance with the light coming from that side.

One way to conceive the principle of the MOT is that the phase-space density (PSD) of the atoms is increased at the expense of the entropy of the laser light is decreased. According to the Liouville theorem an increase in PSD can only be achieved with nonconservative forces such as friction. The highest PSD is obtained for a detuning of $\Gamma/2$, where Γ is the natural line width of the atom. In that case losses are high. Hence, we load the MOT for several seconds with a detuning of 3Γ. Then, we compress it for only a few milliseconds by ramping down the detuning before loading the atoms into the optical trap. We prepare the atoms in the lowest state ($^2S_{1/2}$, $F = 1/2$), by ramping down the power of the cooler faster than the power of the repumper.

Resonator

The resonator is just an intermediate trap that is used to transfer the atoms from the "MOT" into the next trap (see below). Here, the atoms are attracted by a very strong light field. The light is enhanced by a resonator as the sound of a guitar string is amplified by the body of the guitar.

After the atoms were precooled in the MOT, a resonator takes over to confine the atoms. The atoms are trapped due to ac Stark shift, as explained below. The required laser power of several hundred watts is achieved by enhancing the power of a 2 W laser with a resonator.

As the direct transfer of atoms from the MOT into the final trap is not efficient we use a large-volume optical dipole trap as reservoir. A resonator has the advantage of power enhancement and large trapping volume but its disadvantage is the high axial trapping frequency.

Optical dipole trap

Evaporative cooling is used to further slow/cool the atoms . This principal is also used by your body. When you sweat, water is evaporated. Only very fast water molecules can escape from a drop of sweat. Those fast molecules take away a lot of energy and, therefore, cool your body. It is this cooling process that yields the lowest temperatures in the universe. Just cold enough to reach a new state of matter, called Bose-Einstein condensate (BEC). In this state the atoms move as slow as they can possibly do according to quantum mechanics: a few millimeters per second.

As before, the trapping potential is due to the the ac Stark shift which is easy to conceive in the dressed state image. Consider two states: Atom in ground state and P photons in the light field and atom in excited state and $P - 1$ photons. Tuning the laser over resonance the energies of these states cross. They are no more eigenstates of a Hamiltonian that includes atom-light interaction. The new eigenstates show an avoided crossing. For red detuning the eigenstate (adiabatically connected to the ground state) is shifted down. This downshift is proportional to the laser power. Thus, the laser intensity determines the potential.

The ultracold regime is entered by forced evaporative cooling in an optical dipole trap. For most experiments the trap geometry is crucial. A focused laser beam with Gaussian beam profile provides an elongated trap that is not perfectly harmonic. By increasing the laser power, the atoms gather on the bottom of the Gaussian potential that is practically harmonic. For low laser power the axial confinement is dominated by harmonic magnetic confinement because our Feshbach coils are not in Helmholtz configuration. The radial symmetry is broken because the beam is slightly elliptic.

Imaging

A BEC is extremely fragile. Touching it with any material that is not as cold would heat it up and destroy it. It is possible to take an image of the cloud, but only once. The imaging light kicks the atoms out of the condensate and destroys the BEC.

Images of the trapped cloud are called *in situ* and show the distribution in real space. For time-of-flight images, the cloud expands for a certain time before the image is taken which reveals the momentum distribution or the expansion behavior of the cloud depending on the interaction strength.

Absorption images reveal the column density of the atomic sample along the optical axis of the imaging system. To access all axes, we use two imaging systems. One is set up along the trapping beam in order to provide all the radial information.

2.3. Science

Current research: collective excitations

A baby knows how to gain insight into a new object. It chews on it. Thereby, it tests the compressibility. An adult might do it more sophisticatedly. The sound, generated by knocking, also probes the response to a deformation. Modes (that is basically sound in a closed system) are also used to interrogate the properties of a BEC.

We investigate the BEC-BCS crossover by studying collective oscillations. Modes, where the cloud is compressed, are used to prove beyond mean field effects and effects due to the fermionic nature of the constituents of the bosonic dimers made of fermions. Modes, where the surface changes, reveal whether the system is hydrodynamic or collisionless.

Collective modes can be used to test different predictions for the equation of state. This equation reflects many important features of the cloud; e.g. interactions, many-body effects and the Pauli exclusion principle. Properties like compressibility are derived from it and the compressibility determines the frequency of compression modes which can be measured.

Applications

So far you can't find a BEC in any device around you. Also physicists will give you only cryptic predictions of where you'll use it in the future. But 45 years ago none of the physicists developing the laser could answer this question either...

Of course there will be applications for BEC; e.g. precision measurements or matter wave interferometry. But from a scientific point of view, it is most important that ultracold gases serve as a toolbox to simulate and understand many-body systems.

The control over parameters like interaction, trapping potential, spin imbalance and temperature provides a tool to explore the physics of systems that are similar to a neutron star, to heavy nuclei or to high temperature superconductors.

Selected references

The webpage http://www.colorado.edu /physics/2000/bec teaches BEC in a playful way. Some readers might enjoy to get an idea of quantum mechanics. They should be warned that there is no way to understand quantum mechanics without mathematical treatment.

The underlying physics of the experimental procedures is quantum optics [Met99]. BEC is treated in various textbooks [Pet02, Pit03] and more experimentally in review articles [Ket99]. The basis of crossover physics was introduced by Leggett [Leg80, Noz85].

The technical features of the experiment are documented in previous diploma theses [Joc00, Hen03, Rie04] and Ph.D. theses [Joc04, Bar05]. For our major scientific contributions we refer to some publications [Joc03, Chi04, Alt07] which were recently summarized in [Gri].

3. Motivation for Experimental Upgrades

In this section the implementation of two technical innovations for our experimental setup is motivated. First, we present an overview of how we create an ultracold atomic sample in a trap. Then we briefly discuss interaction in this sample, come to problems of current research and list several experiments for investigation of those problems. These experiments suggest the implementations of a trap that can be moved and deformed and the construction of a new imaging system.

In a sequence of essentially four stages, we create an ultracold cloud of fermionic ^{6}Li atoms [Gri]. The first two stages use the radiation pressure of resonant light [Met99]. An atomic beam of ^{6}Li atoms is decelerated by a Zeeman slower so that the atoms are captured in a magneto-optical trap (MOT) [Joc04]. These methods have become standard and are described in [Met99]. The next two stages take advantage of the ac Stark shift of the atomic ground state energy that is induced by far detuned light. This shift, which is proportional to the light intensity, determines the potential of an optical dipole trap [Gri00]. For red detuning the ground state energy is decreased and the atoms are attracted towards higher light intensity. After the MOT has been loaded, such a dipole trap takes over to confine the atoms. To avoid losing atoms in this transfer, a large trapping volume of sufficient potential depth is required which can be achieved using a resonator [Els00, Mor01]. This resonator-enhanced dipole trap serves as a reservoir from which atoms are loaded into a tighter dipole trap formed by a single focused Gaussian laser beam. The light intensity distribution of this trapping beam leads to a nearly cylindrically symmetric trapping potential. The trap is much steeper in the radial direction than it is in the longitudinal direction along the axis of the beam, i.e. the radial trap frequency is higher than the axial trap frequency and the atoms form a cigar-shaped cloud, as shown in Fig. 3.1. This optical dipole trap allows for forced evaporative cooling as we decrease the potential depth by reducing the power of the laser beam [Joc04]. At this stage, cooling is completed.

Apart from temperature, two-body interaction is crucial in our experiment. The elastic interaction between two ultracold atoms can be characterized by a single parameter, the s-wave scattering length a. As a function of magnetic field strength, a has a pole at a magnetically tuned scattering resonance, known as Feshbach resonance [Ino98] where a bound state energy level crosses the threshold energy when tuning an external

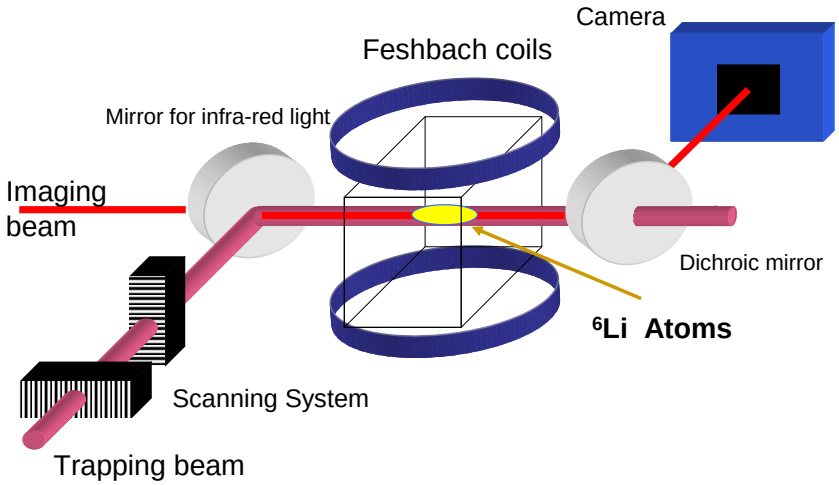

Figure 3.1.: Sketch of our experiment. Components needed for the creation of the ultracold gas are left out. The coils provide the magnetic field to tune the two-body interaction of the atoms via a magnetic Feshbach resonance. The atoms are confined in the potential of an optical trap formed by a focused laser beam. This beam can be steered by a scanning system. The imaging beam is aligned along the trapping beam. After the first mirror the beams overlap and the second dichroic mirror prevents the trapping light from reaching the camera.

magnetic field. The two lowest spin states in our two-component spin-mixture of ^{6}Li atoms show a wide Feshbach resonance with the center at 834 G. Below resonance, two atoms can decay into a weakly bound state by three-body collisions and form a bosonic molecule [Joc04]. Above resonance, the scattering length is negative which stands for attractive interaction where pairing can occur due to a different process as mentioned below. Close to resonance, the interaction is strong, i.e. the scattering length is larger than the mean inter-particle spacing.

The control over temperature and interaction allows to generate various states of interest in our experiment. These states, which are still difficult to treat theoretically, lie in between several states, which are known from theory and various experiments:

- Bose-Einstein condensation (BEC) of a trapped Bose gas is the macroscopic occupation of the ground state of the trap below a critical temperature. The condensate is superfluid when the particles interact [And95, Pet02, Pit03].
- The macroscopic occupation of a motional state, as it occurs in BEC, is forbidden for fermions because of the Pauli exclusion principle. At low temperatures, fermions arrange themselves in the lowest states of the trap and form a so-called Fermi sea.
- The Bardeen-Cooper-Schrieffer (BCS) theory describes a transition to a superfluid at zero temperature for fermions with weak attractive interaction by forming Cooper pairs [Bar57, Kup68].

All these theories assume weak interaction in contrast to strong interaction where a is of the order of or larger than the inter-particle spacing. The experiment also runs at finite temperatures. Thus the regimes that we access experimentally can only be associated with those states.

In the following we briefly discuss the regimes in a sweep of magnetic field strength across the Feshbach resonance. Starting from well below the resonance, we create a molecular BEC of weakly bound, but stable, ^{6}Li dimers [Joc03]. Ramping the magnetic field strength over resonance, pairing persists [Chi04] but changes its nature. The pairing is no more a molecular binding but changes smoothly to a BCS-like pairing when the interaction becomes attractive. Throughout this so-called BEC-BCS crossover, the atom cloud behaves superfluid. For a further increase in magnetic field, the pairing gap decreases and drops below the thermal energy. That is why superfluidity is expected to break down. The collision rate is still high and the collisions favor a hydrodynamic regime [Coz03]. For an even higher magnetic field strength, collisions are Pauli blocked and a Fermi sea forms. Thus we cross three regimes which can be distinguished by their dynamics. The superfluid in the crossover cannot support vorticity as long as no quantized vortices are excited and behaves irrotationally hydrodynamically [Pet02]. The collisional Fermi gas is described by normal hydrodynamics and the Fermi sea is collisionless.

Subject to current research is to distinguish whether the atom cloud behaves in a superfluid, normally hydrodynamic or collisionless way depending on the interaction. Various properties can serve as distinctive features:

1. A superfluid has to form vortices in order to carry angular momentum [Mat99]. Conversely, vortices serve as a direct proof of superfluidity. For a strongly interacting fermionic gas, this proof was used in [Zwi05].

2. Two colliding matter waves show interference as a signature of long range coherence [Shi04]. Coherence is a necessary but not sufficient condition for superfluidity.

3. The expansion of an atom cloud from a trap depends on the pressure gradient when the gas is hydrodynamic and on the initial momentum distribution when it is collisionless [Men02].

4. Collective excitations can be used to study the transition either from the hydrodynamic to the collisionless regime or from the normally hydrodynamic to the superfluid regime [Coz03]. Since the frequency of an oscillation can be measured very precisely, collective excitations are a precise quantitative tool.

We shall see that all those experiments can be realized by deforming and/or moving the trap.

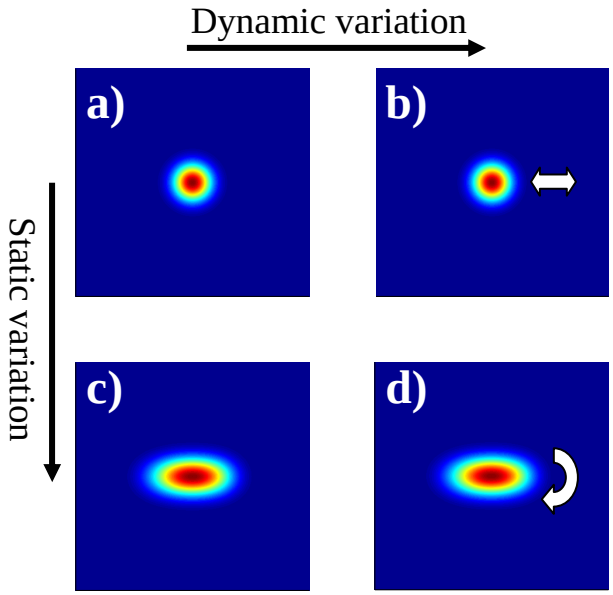

Figure 3.2.: The normalized potential depth is illustrated in a plane perpendicular to the propagation axis of the trapping beam. a) shows the unchanged potential, b) and d) indicate a motion and a rotation. In c) and d) the shape of the potential is varied.

1. To create vortices, angular momentum must be transferred to the cloud. Therefore, the trap is deformed to provide an elliptic potential and then rotated as indicated in Fig. 3.2 d).

2. For interference, two atom clouds have to overlap. E.g., this is realized when two clouds expand from a double well potential.

3. The difference in hydrodynamic and collisionless expansion can be directly seen on time-of-flight images when the pressure gradient varies for different directions. This applies for an elliptic trap as illustrated in Fig. 3.2 c).

4. Collective excitations are initialized whenever the cloud is in a non-equilibrium position or shape with respect to the potential. As an example, the dipole mode where the center of mass sloshes is excited by changing the center position of the trap as shown in Fig. 3.2 b).

These experiments should motivate the realization of a trapping potential that can be varied dynamically and statically. Dynamic variation refers to motion or rotation and static variation refers to deformation.

The basic concept is that both types of variation can be accomplished by just moving the trapping beam. This is clearly evident for changing the center position of the potential as shown in Fig. 3.2 b). The static variation in potential corresponds to a time-averaged potential [Fri00, Mil01]: The trapping potential is calculated from the

laser light intensity. As long as the trapped atom is at a fixed position, we can time-average a fast varying potential to an effective potential. We introduce the condition that the atom must stay at its position within w/c where w is the radius of the trap and c the strictness of the condition that will be experimentally acquired. This is fulfilled in the time interval $\tau < 1/(c \times \omega)$ because the fastest atoms in such a trap have the velocity $v = w\omega$, where ω is the trap frequency. Thus, we just superimpose all potentials in the time interval τ to get the time-averaged potential. Furthermore, we have to make sure that no eigenmodes of the trap are excited to avoid heating. An oscillator does not absorb energy from an external force when the driving frequency of the force is well above the eigenfrequency of the oscillator. The eigenfrequencies of the atom cloud are of the order of ω. The inequality from above gives a lower bound for the driving frequency $1/\tau > c \times \omega$. It follows that c has to be much bigger than 1 and in experiments we could verify that there is no heating for $c > 100$. To clarify this, we give an example of how we generate a time-averaged potential. The trapping beam moves periodically along a closed track with a period less than τ. Then the atoms feel a trap potential that is given by the laser power averaged over one period. E.g., the potential in Fig. 3.2 c) is generated by moving the beam from left to right and back within one period. Such quasi-static potentials can also be realized in a magnetic trap [Hod01].

To introduce a coordinate system, we define the z-axis to be along the trapping beam. For all the experiments mentioned above, it is sufficient to move the beam along the x- and the y-direction. This corresponds to a parallel translation of the trapping beam and can be accomplished by deflecting it. For deflection we use two acousto-optic modulators (AOMs); one for deflection in x-direction and one for deflection in y-direction as shown in Fig. 3.1. Because of this two-dimensional positioning of the beam the setup is called scanning system.

The experiments work with a dynamic and static variation of the potential in the x-y-plane. Accordingly, the response of the cloud, e.g. expansion or oscillation, is pronounced in this plane. To measure this response we use absorption imaging [Ket99]. Only an imaging system along the trapping beam yields full information on the cloud profile in the x-y-plane (see Fig. 3.1). This orientation of the imaging system comes with two challenges:

- No light of the trapping beam may shine onto the camera. Besides dichroic mirrors, as shown in Fig. 3.1, we have designed and implemented a very fast shutter (see appendix A.2).
- The trapping beam enters the vacuum glass cell at an angle close to the Brewster angle. Therefore we image through a tilted glass plate. This induces aberrations that we have to compensate in order to visualize small objects (like vortices or interference fringes) and to get unblurred images of the cloud profile.

The scanning system and the imaging system provide a powerful toolbox for investigation and are documented in the following sections.

4. Design and Implementation of Two Experimental Upgrades

In the previous chapter, we have listed experiments which motivated the implementation of a scanning system and a new imaging system. This chapter discusses the technical background and the performance of these upgrades.

4.1. Scanning System

The final stage in our experiment is the optical dipole trap formed by a single focused laser beam. This chapter is a detailed discussion of how to set up this trapping beam so that it provides efficient production of a sample of ultracold atoms and the ability to move and to change the shape of the trapping potential. After loading this trap with atoms from a large-volume, resonator-enhanced dipole trap, we lower the trap depth by reducing the power of the laser beam and, thus, force evaporative cooling. The trap size and maximal depth are optimized with respect to loading and cooling efficiency in order to obtain as many and as cold atoms as possible. The trapping beam is not

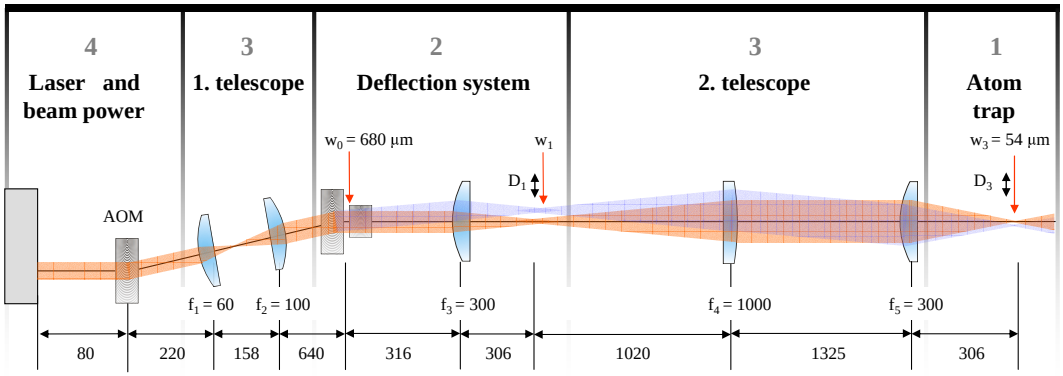

Figure 4.1.: We group the components of the scanning system into five sections of four topics ($X = 1, 2, 3, 4$), discussed in section 4.1. X, respectively. AOMs are used for controlling the beam power and for deflection. Telescopes adjust the beam parameters for deflection and trapping. The numbers on bottom have the unit of length in millimeters.

only used to prepare the sample of ultracold atoms, but it also provides the trap for all our experiments. The scanning system allows for dynamic or static variations of the trapping potential. This is achieved by deflecting the trapping beam using acousto-optic modulators (AOM). A fast modulated deflection results in a quasi-static potential for the atoms as motivated and explained in the previous chapter.

The setup is grouped into six sections, as shown in Fig. 4.1. First we will introduce all the parameters that are crucial for the atom trap. Then we will see that all the requirements on deflecting the beam can be achieved with AOMs. The subsequent sections are rather technical and briefly discuss the telescopes, the laser and the power control. We conclude with summarizing the performance of the scanning system.

4.1.1. Atom trap - Deducing requirements on the scanning system

In this section, the crucial parameters for the trapping beam and the deflection system are defined and quantified.

For all experiments it is desirable to prepare a large number of ultracold atoms. The parameters of the single focused laser beam are subject to the optimization of cooling and loading. With this given beam we want to create various trapping potentials. The requirements on the deflection system are motivated by a few selected potentials.

Beam parameters

The trapping potential formed by the Gaussian trapping beam with given detuning is calculated using two parameters: the beam waist w_3 and the intensity I [Gri00]. For given maximal power of the laser beam, I scales as $1/w_3^2$. The beam waist is a crucial parameter to optimize particle number and cooling efficiency.

A tight trap (small beam waist) has the advantages of

- efficient cooling since the strong confinement of the atoms leads to a high density resulting in a high collision rate,
- high phase-space density at given temperature due to the high density,

compared to the advantages of a shallow trap (large beam waist) which provides

- efficient loading from the resonator because the volume of overlap is large
- small anharmonicity for given trap frequency. This applies to the recompressed trap after completed evaporation.

As a trade-off between these factors we compromised on a beam waist of about 55 μm. This is based on measurements with beam waists of 35, 45 and 80 μm. The atom

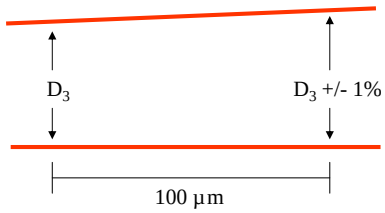

Figure 4.2.: Tilting is a measure for the uncertainty in amplitude of translation. It is convenient to define it over a distance of 100 μm which is the typical length of the atom cloud.

number is monitored during transfer and evaporation in our typical BEC experiment [Joc04]. At the end of evaporation this number shows a plateau and drops immediately for further lowering of the trap depth. The number of atoms on the plateau is interpreted as twice the number of molecules in the BEC. This number is a measure for loading and cooling efficiency. Thus, it is used to find the trade-off.

For small power of the laser beam, the axial confinement is dominated by the curvature of the magnetic field of the Feshbach coils. Thus, the dependence of the axial confinement on the beam waist needs not to be taken into account. Also the various potentials we want to create by deflection of the beam were not part of this discussion. A smaller beam waist would enable us to write time-averaged potentials with smaller structure and steeper potential walls.

Parameters for deflection

The requirements on deflection follow from various potentials which we want to create with the trapping beam, the waist of which is optimized for the production of ultracold atoms. The desired potentials named here are explained in more detail in chapter 5.

The deflection will be converted into a parallel translation of the beam as can be seen in Fig. 4.3. We find three crucial parameters for this translation:

1. Resolution R - This is the number of resolvable spots. As the size of one spot is the beam diameter $2w_3$ and the amplitude of translation is defined as D_3, the resolution is given by $R = D_3/2w_3$. It is not changed by a telescope.

2. Bandwidth of deflection BW - The angular modulation frequency where the amplitude of deflection has dropped by 3 dB.

3. Tilting with translation Π - We define Π as the percentaged change in amplitude of translation over a certain distance as shown in Fig. 4.2.

We deduce values for the parameters of translation by considering the most critical experiments for the respective parameter:

1. Of all the potentials we want to create, the double well, where we want to split the atom cloud as shown in Fig. 5.1 c), requires the largest R. For full separation we demand $D_3 > 4w_3$, i.e. $R > 2$.

2. Consider the creation of an elliptic potential as shown in Fig. 5.1 b). A modulation frequency close to the trap frequency $\omega_\perp$ excites and heats the atoms. Prior experiments have shown that there is no heating for modulating 100 times faster. This gives $BW > 100 \times 2\pi \times 500$ Hz where a typical $\omega_\perp$ was inserted. Even larger BW would permit the creation of more complex patterns. In case of addressing a grid of points, this is analog to the deflection of a cathode ray in a television. The vertical sampling rate is faster than the eye would be able to track but the horizontal sampling rate is even faster.

3. In case of $\Pi \neq 0$, the trapping potential is changed differently at the front end and at the back end of the cigar-shaped cloud. We consider the excitation of rotation using a rotating ellipse (see Fig. 5.1 e)). The induced angular momentum depends on the ellipticity of the potential and should be constant along the cloud. As a criterion we demand $\Pi < 1$ % over the typical length of the atom cloud, as illustrated in Fig. 4.2.

4.1.2. Deflection with AOMs

This section is devoted to one possible realization of a deflection system. We show that the requirements on translation, introduced above, can be met using AOMs. We refrained from other approaches to deflect or even deform the trapping beam, e.g. by using a spatial light modulator, because of poor modulation bandwidth and because of the high power of the laser.

Fig. 4.3 shows the deflection by an AOM for one axis of translation. In this setup the beam waist w_0, the focal length f_3 and the center frequency of the AOM f_m are free parameters. A relation to the required resolution is derived in the following excursion. Note that the second telescope does not change the resolution.

Excursion 1 *To see how the resolution depends on the AOM we start with the definition of the resolution*

$$R = \frac{D_1}{2w_1}, \tag{4.1}$$

and eliminate

- w_1 *by using Gaussian optics* $w_1 = \lambda f_3/(w_0\pi)$,
- w_0 *by introducing the time it takes for a sound wave to cross the beam* $T_s = 2w_0/c_s$,
- c_s *by expressing it in terms of* λ_s *and* f_m,

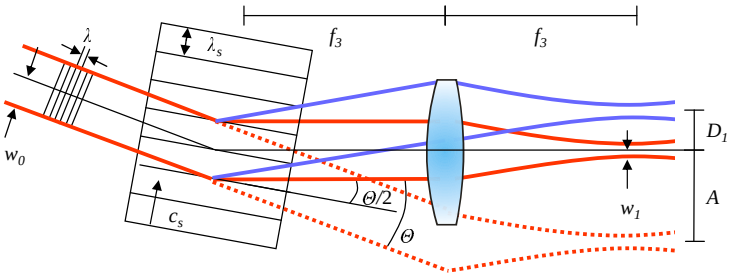

λ	Wavelength of light
w_0	Waist at AOM
w_1	Waist in focus
λ_s	Wavelength of sound
c_s	Speed of sound in crystal
Θ	Angle of deflection
f_3	Focal length
A	Translation relative to 0. order
D_1	Translation for $\Delta f = BW_{AOM}$

Figure 4.3.: An AOM deflects light using sound waves. The lens converts this angular deflection to a parallel translation. The frequency of sound f can be varied around the center frequency f_m within the bandwidth of the AOM, BW_{AOM}. At the edges of this bandwidth the efficiency of deflection is decreased by 3 dB. BW_{AOM} is not to be confused with BW that corresponds to the frequency of how fast f is changed. A sweep over the full BW_{AOM} leads to a deflection D_1. The resolution is $R = D_1/(2w_1)$.

- *λ_s by using Bragg's condition for the angle of deflection $\theta/2 = (\lambda/2)/\lambda_s$,*
- *f_m with the relation that the bandwidth of the modulation amplitude BW_{AOM} to f_m behaves like D_1 to A,*
- *A by using $\theta = A/f_3$.*

A relation between the resolution and the time bandwidth product, which can be found in data sheets, is left.

$$R = \frac{\pi}{4} T_s BW_{AOM} \tag{4.2}$$

Undoing the second step from above gives the interesting result that the resolution depends only on intrinsic properties of an AOM and the beam waist:

$$R = \frac{2\pi}{4c_s} w_0 BW_{AOM} \tag{4.3}$$

We choose the AOM 3110-197 from Crystal Technology. The speed of sound is 4200 m/s and 3dB-BW_{AOM} is 25 MHz which is strongly related to the operation frequency $f_m = 110$ MHz. Thus, the beam waist has to be larger than 220 μm to fulfill $R > 2$. To increase the diffraction efficiency we choose $w_0 = 680$ μm. Furthermore, with this w_0 it is possible to stay within the 1dB-BW_{AOM} to get $R \approx 2$.

One can calculate the crossing time $T_s = 0.3$ μs which can be converted into BW: Assuming that two sequential sound waves have to cross the beam to complete one cycle of deflection we get $BW = 2\pi \times 1.6$ MHz. This fulfills the requirement but in practice BW is limited by electronics, as specified later.

4.1.3. Telescopes - Adjusting parameters of the system

We have seen that, for a given AOM, the deflection parameters R and BW are translated into the beam parameter w_0 at the position of the AOMs. Thus, almost all crucial parameters of the system, deduced in Sec. 4.1.1, are adjusted with telescopes. One parameter left is tilting.

The first telescope provides w_0. The lens behind the AOMs gives w_1 which is to be converted to w_3. Besides that, the second telescope also has to preserve parallelism of translation ($\Pi = 0$). Only then the resolution R is preserved. This requires a confocal configuration leaving no degree of freedom for adjustment of the second telescope because f_5 is limited for experimental reasons. Tilting can only be zero if the AOM is in the focal plane of the subsequent lens. This is not possible for two AOMs. The AOM before (behind) this plane leads to negative (positive) Π that cannot be changed by changing f_3 and the second telescope.

4.1.4. Laser and beam power

We use an ELS VersaDisk laser with an output power of 26 W at a wavelength of 1030 nm. The ellipticity of the beam is typically about a few percent. For evaporative cooling the power of the beam has to be controlled over four orders of magnitude. This cannot be done with one of the AOMs used for deflection because the stray light from the crystals of these AOMs is collimated at the position of the atoms. The stray light cannot be dumped without cutting light of the trapping beam when deflecting. It is estimated to be of the order of a milliwatt on the area of the dipole trap, only one order of magnitude below the power of the laser beam at the end of evaporation. A third AOM, of which the stray light can be extinguished, is used for attenuation.

4.1.5. Performance of the scanning system

Having discussed all components we test the performance of the scanning system. The results are summarized in Tab. 4.1 below.

Earlier on, the typical ellipticity of the laser beam was mentioned. It is expected to change when the beam is deflected by an AOM; furthermore, astigmatism induced by imperfect alignment of lenses might add ellipticity. An elliptic beam has two principal axes, named x' and y'. The ellipticity is defined as $\epsilon = (w_{x'} - w_{y'})/\sqrt{w_{x'} w_{y'}}$. The values in Tab. 4.1 are derived from trap frequency measurements as presented in chapter 5.1.

Translation amplitude D_3', bandwidth of deflection BW and angle of the AOM axes relative to the imaging axes δ were derived from *in situ* images of experiments where the atom cloud was split into four parts (see Sec. 5.4.), as shown in Fig. 4.4. In this experiment D_3' is chosen to correspond to $R \approx 1$ but the translation can be increased to give $R > 2$. The relative difference in D_3' is to be compensated by multiplying the ap-

Table 4.1.: Parameters characterizing the scanning system. The orientation of the principal axes of ellipticity x' and y' are not of interest. The beam has an ellipticity ϵ. The axes x and y correspond to the direction of deflection of the AOMs. The relative translation is the ratio of translation in x and y direction and the relative angle is the angle between the axes of deflection.

		x'	y'	ϵ
Beam waist	w_3	52 μm	56 μm	7 %
		x	y	relative
Translation	D'_3	104 μm	116 μm	90.4 %
Modulation bandwidth	3dB-BW	950 kHz	1100 kHz	-
Deflection angle	δ	33.4°	32.9°	89.5°
Tilting	Π	< 0.5 %	< 0.5 %	-

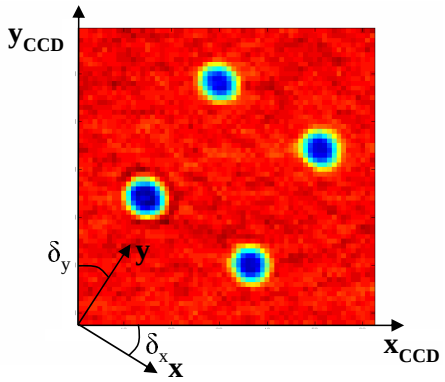

Figure 4.4.: The cloud is split into four parts as discussed in Sec. 5.4. Positions of the parts are used to characterize the angles (δ_x and δ_y) of the axes of deflection (x and y) relative to the CCD axes (x_{CCD} and y_{CCD}) and the translation. The amplitude of translation is adjusted by the peak-to-peak voltage of the wavefront generators and the multiplication voltage on the corresponding control channel (here 2 V and 3 V, respectively).

propriate control channel with 0.904. The angle between the axes of deflection is close to 90°. 3dB-BW is gained from the decrease in D'_3 when increasing the frequency of modulation. It is limited by the electronics driving the AOM and not by the theoretical limit that is $BW = 2\pi \times 1.6$ MHz.

For a measurement of tilting the beam is reflected before entering the glass cell, enabling direct access. A pattern, also used for Fig. 4.4, was directly imaged for different positions before and behind the focus. These images provide D_3 as a function of the position along the beam and thus the tilting.

It was shown that the scanning system using AOMs for deflection meets all the requirements stated above. This setup is used to create customized potentials for a variety of experiments, as discussed in the next chapter.

4.2. Imaging System

Imaging of ultracold atoms resolves two dimensions of the density of a sample. The three-dimensional density is integrated along the optical axis which results in the so-called column density. In many experiments, especially when using the scanning system, we are mainly interested in the column density along the two radial dimensions of the trap. Therefore, we set up an imaging system of which the optical axis coincides with the longitudinal axis of the trap, i.e. along the trapping beam. Among other methods like fluorescence or dispersion imaging, absorption imaging [Ket99] is particularly suited for our experiment because of the relatively low number of atoms. We detect the partially absorbed, resonant imaging laser beam with a CCD camera, as sketched in Fig. 3.1.

We start with a discussion of resolving power and signal to noise. This leads to a preliminary design of the imaging system as if it was diffraction-limited. Then, we introduce the wavefront formalism in order to deal with the aberrations that are induced by the tilted glass cell. In the final imaging system we compensate these aberrations. Using artificial objects instead of the atom cloud, the imaging system is characterized.

4.2.1. Design of a diffraction limited imaging system

We consider an imaging system where the performance is limited by diffraction and the image is recorded with a CCD camera. The system consists of two lenses in a confocal configuration, meaning that the light coming from the object is collimated in between the lenses and that the lenses are spaced by the sum of their focal lengths f_1 and f_2. The geometry of this system is characterized by three parameters: The pixel size of the camera p, the relative aperture A which is defined as the focal length over the diameter of the first lens, $A = f_1/D$, and the magnification $M = f_2/f_1$. The performance of this system is characterized by the minimum resolvable distance d or g and the signal-to-noise ratio SNR. We will see that finding the right geometry is a trade-off in the parameters of performance.

Resolving power

Two different approaches to the minimum resolvable distance can be found in literature [Hec90].

- Most known, the Rayleigh criterion defines the diffraction patterns of two point sources in the image plane as resolved when the center of one is located in the diffraction minimum of the other, as is the case in Fig. 4.5 a). Behind a round aperture, the diffraction pattern of one point is described by an Airy function. The distance from the zeroth maximum to the first minimum is $d' = 1.22\lambda A'$ where A' is the relative aperture of the second lens and λ is the wavelength. The

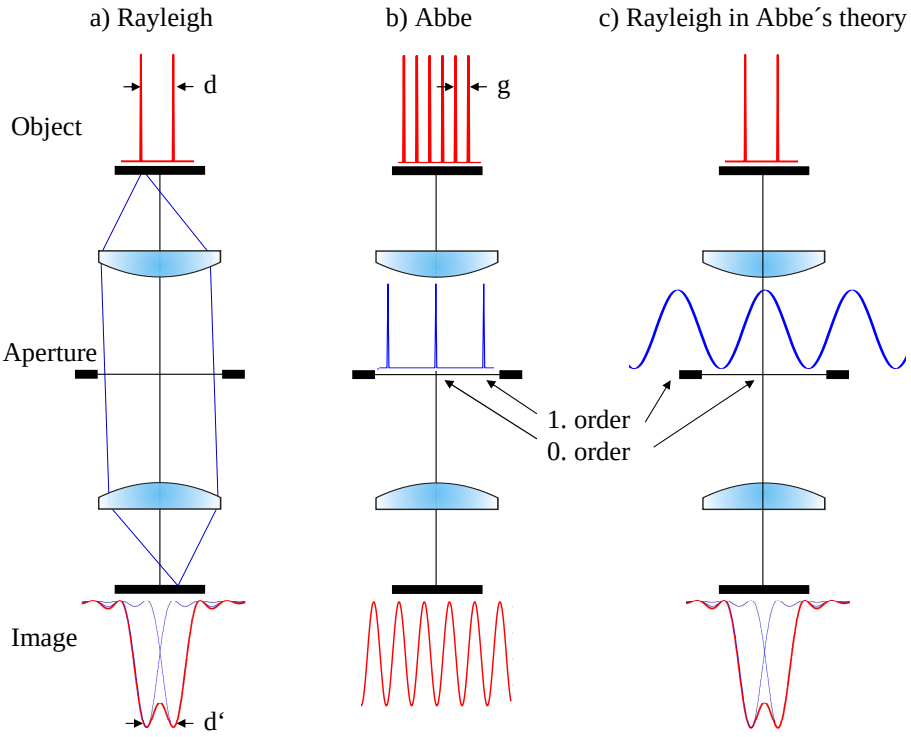

Figure 4.5.: Two different resolving power criteria, according to Rayleigh (a) and Abbe (b). The right image shows Rayleigh's criterion transcribed into Abbe's theory. The objects are resolved as long as light of the first order can enter the aperture. All curves are intensity profiles.

prefactor models the geometry of the aperture. The minimum resolvable distance in the object plane is $d = d'/M = 1.22\lambda A$ where we have used $A = A'/M$.

- Abbe argues the other way round and considers the smallest possible object. A grating with spacing g, illuminated from the back (from above in Fig. 4.5 b)), can be resolved if light from the first order of diffraction enters the lens system. That is true for the minimal spacing corresponding to the minimum resolvable distance $g = 2\lambda A$.

The arguments for the two criteria have different starting points, the image and the object plane. Nevertheless, they should lead to the same result for the minimum resolvable distance d and g, respectively. Considering that Abbe does not take into account that the aperture is round, a factor of 2 is missing in the Rayleigh criterion. The answer can be found by starting Rayleigh's problem in the object plane, as illustrated in Fig. 4.5 c). One can see in the Fourier plane that, for non periodic objects, the first order has tails entering the aperture, although the peaks are cut off. The light in the first order causes destructive interference that yields a minimum in between the two images of the two point sources resolving them. This is valid as long as one is working

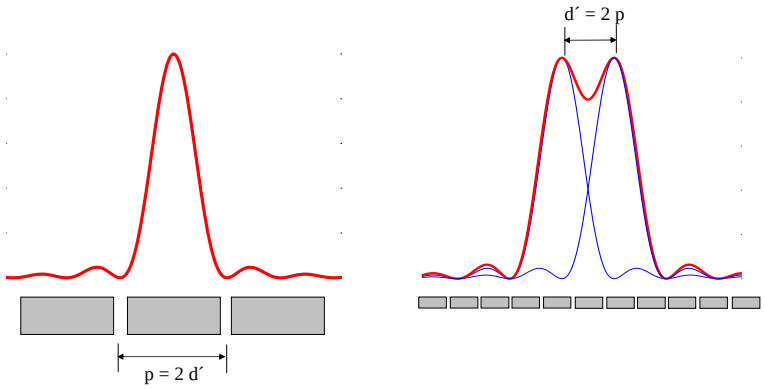

Figure 4.6.: The huge pixels meet the signal to noise criterion, as the light of the zeroth order is concentrated on one pixel. The Rayleigh criterion requires four times smaller pixels.

without high spatial frequency. The Abbe criterion is valid, for experiments where, for example, interference fringes are to be resolved.

Until now, we did not consider the pixel size p. The Rayleigh criterion requires $p < d'/2$ since the minimum between the points has to be detected as shown in Fig. 4.6. Bigger p would limit the effective resolving power of the imaging system to $d_{eff} = 2p/M$.

Signal-to-noise

Besides resolving power, the signal-to-noise ratio governs the performance of the imaging system. Excursion 2 shows that SNR is best when all the light coming from a point source is focused on one single pixel.

Excursion 2 *Let S photons shine onto x pixels. Every pixel has N counts due to noise. Signal and noise obey Poissonian statistics resulting in a deviation of $\sqrt{S/x}$ and $\sqrt{N}$ respectively. This statistically adds up to $\sqrt{S/x + N}$ per pixel. Summing and averaging this deviation over x pixels gives the deviation of the signal $x/\sqrt{x} \times \sqrt{S/x + N} = \sqrt{S + x \times N}$. Thus, the smallest error in measuring S, the best signal-to-noise $SNR = (S/\sqrt{S + x \times N})$, is achieved when detecting with only one pixel.*

Even in an aberration-free imaging system, the light of a point source is spread out in the image plane due to diffraction. The main fraction of light (84%) is contained in the zeroth order of the diffraction pattern (Airy function). To capture this fraction on only one pixel, the pixel size must be $p = 2d'$, as shown in Fig. 4.6. In this case the effective resolving power is four times below the optimum resolving power given by the Rayleigh criterion. A trade-off between effective resolving power and SNR has to be found.

Table 4.2.: The effective minimal resolvable distance is limited by the Rayleigh criterion for the magnification $M = 8$. The signal-to-noise ratio is better for less magnification. The values chosen for our experiment are given in the right column.

optimized for	Resolving power	Signal-to-noise	Experiment
d_{eff}	3.3 μm	13 μm	8 μm
M	8	2	3.2

Design of the imaging system in our experiment

Above, we have found two relations between the pixel size p and the minimal resolvable distance in the image plane d', as shown in Fig. 4.6. We will use these relations to design the imaging system in our experiment where the following parameters are given: The wavelength is $\lambda = 0.671$ μm, the pixel size of the CCD camera is $p = 13$ μm and the relative aperture of the first lens is $A = 4$ which is limited by optical access to the vacuum chamber. With these parameters we calculate the minimal resolvable distance in the object plane $d = 3.3$ μm according to the Rayleigh criterium. From that the magnification for a system optimized for resolving power follows, as shown in Tab. 4.2. To optimize signal-to-noise the magnification is four times less and d_{eff} is four times worse. We have chosen the values given on the right side of the table. We cannot reach the optimum resolving power of 3.3 μm anyway due to random and systematic aberrations, as discussed later.

4.2.2. Optical aberrations induced by a tilted glass plate

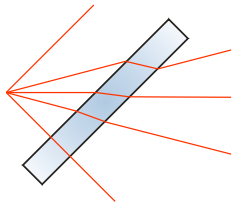

Figure 4.7.: A tilted glass plate leads to a displacement of the beam that does not scale linearly with its angle of incidence.

Many features of interest of an atom cloud, e.g. vortices or interference fringes, could be created with the scanning system and, thus, would show up in the column density along the axis of the trapping beam. That is why the imaging system is on-axis with the trapping beam. To maximize loading efficiency, this beam has a small angle relative to the resonator that has to be aligned with the Brewster's angle relative to the vacuum

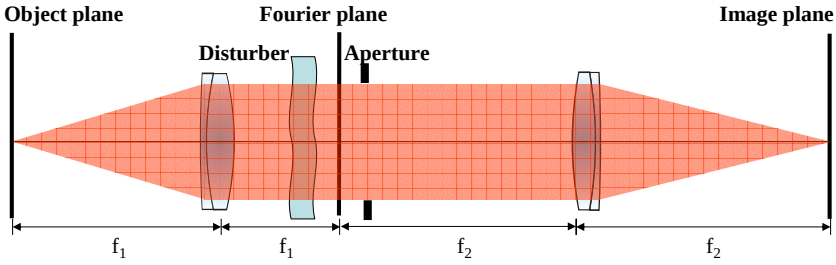

Figure 4.8.: In a confocal imaging system, the Fourier plane coincides with the rear focal plane of the first and the front focal plane of the second lens. The light of one point source that passes the aperture is shaded.

glass cell in order to minimize loss in light power. Thus we image through a tilted glass plate - aberrations are induced and the system is no more diffraction limited as assumed above. In the following excursion, the reader should get a simple picture of why a tilted glass plate causes aberrations to a not collimated beam. Then we will address the problem in terms of wavefront analysis.

Excursion 3 *A ray passing through an inclined coplanar medium exhibits a phase shift and a displacement. For a collimated beam this affects all rays the same and does not cause aberrations. But in a diverging or converging beam, the rays enter the plate with different angles. Since displacement and phase shift are described by trigonometric functions they are nonlinear and the beam is changed in a complex way.*

Brief introduction to wavefront analysis

To describe aberrations, we move from the ray picture to the wavefront picture. In addition to the object and the image plane, we introduce the Fourier plane [Hec90], as shown in Fig. 4.8.

In all three planes the light field is described by a complex function

$$\mathbf{E} = E(\rho, \theta)e^{i\phi(\rho,\theta)}, \tag{4.4}$$

where ρ and θ are polar coordinates, ρ is dimensionless and normalized so that it is 1 at the edge of the aperture. E is the amplitude of the electric field and ϕ is its phase. From this phase, we can calculate a surface of constant phase, called wavefront. The light field in the Fourier plane is the Fourier transform (FT) of the light field in the object plane and the inverse FT is used to go from the Fourier to the image plane. In the object plane the imaging light (approximated by $\mathbf{E} = 1$) is modified due to absorption and dispersion of the object. In the Fourier plane, the aperture cuts off the amplitude. When using a CCD camera, only the intensity, the square of the absolute value of $\mathbf{E}$, matters in the image plane. This formalism is explained in various textbooks on optics, e.g. [Hec90].

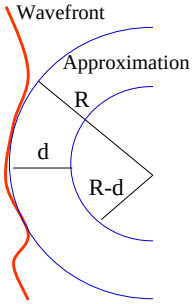

Figure 4.9.: An arbitrary wavefront is locally approximated by a sphere with radius R.

A perturber in the Fourier plane, as sketched in Fig. 4.8, induces an additional phase shift to the light field in the Fourier plane. If the position of such a perturber is outside the Fourier plane, auxiliary planes must be introduced and transforms of the light field from one plane to the next become complicated. We will show in the next excursion that sufficiently small aberrations, anywhere between the two lenses, can be shifted into the Fourier plane, making analysis simpler.

Excursion 4 *Any wavefront curvature can be locally approximated by a curvature with radius R, as shown in Fig. 4.9. R corresponds to a focal length. When the wavefront propagates for a distance d the radius changes to $R - d$. Hence the wavefront stays unchanged if $d \ll R$. This approximation is fulfilled for our values, as can be seen later.*

It is convenient to expand the wavefront in a series of polynomials that can be related to known kinds of aberration like astigmatism, coma and spherical aberration [Wya92]. One such set are the Zernike polynomials. The first nine polynomials are listed in Tab. 4.3. Neither an overall shift nor a displacement of the focus due to tilt or defocus cause aberrations. Only polynomials describing the abbreviation from a spherical wavefront, numbers 4-8 in the table, are considered in the following. Higher order polynomials are neglected.

Analysis of the aberrations

In our imaging system, the glass cell, which has an angle of about 45° relative to the optical axis, is the perturber which induces aberrations, as shown in Fig. 4.12. We quantify the aberrations theoretically and check if the predictions match experimental data. If so, we can move on to the compensation of the aberrations.

For testing, we have set up an imaging system with the same optics as in our machine but with a smaller pixel size. The glass cell is replaced by a high-quality glass plate. Unlike in the machine, where the object plane is in the vacuum chamber, it is now possible to work with well defined artificial objects. We use pinholes with a diameter

Table 4.3.: The first nine Zernike polynomials are listed using polar coordinates. The polynomials are dimensionless and give the deviation in multiples of a wavelength. One wavelength corresponds to a phase shift of 2π.

Number	polynomial	related to
0	1	shift
1, 2	$\rho\cos\theta$, $\rho\sin\theta$	tilt
3	$2\rho^2 - 1$	defocus
4, 5	$\rho^2\cos 2\theta$, $\rho^2\sin 2\theta$	astigmatism
6, 7	$(3\rho^2 - 2)\rho\cos\theta$, $(3\rho^2 - 2)\rho\sin\theta$	coma
8	$6\rho^4 - 6\rho^2 + 1$	spherical aberration

Table 4.4.: The coefficients, calculated with *Zemax*, are to be multiplied with the respective Zernike polynomials, as listed in Tab. 4.3. This gives the change in wavefront, namely the deviation from a spherical wavefront, due to the glass plate. Coefficients with odd number do not contribute because we have chosen the tilting axis of the glass plate to be around an axis with $\theta = 90°$ which preserves the symmetry axis along $\theta = 0°$.

Zernike coefficient number	4	5	6	7	8
Coefficient	7.1	0	1.3	0	1.7

ranging from 5 μm to 20 μm that are illuminated by a laser. Experimentally, it is hard to measure the wavefront directly. It is much easier to take an image in the image plane. On the one hand such an image is much more informative in terms of resolving power. On the other hand it does not give a clue which kind of aberration is causing the perturbation. We use these images to verify the theoretical calculation of aberration which reveals the kind of aberration.

Our calculation starts with the computation of the change in wavefront due to the glass plate using the software package *Zemax*. The result, expressed in Zernike coefficients, is given in Tab. 4.4. One can argue that the change in wavefront does not depend on the exact position of the glass plate (since the convergence does not change between object and first lens, the effect to every ray is the same no matter where the glass plate is which leads to the same wavefront). Thus, we have the change in wavefront at the first lens and, with the approximation in excursion 4, we simply shift it into the Fourier plane. There it is added to the phase of the light field.

This prediction of the wavefront now has to be compared to an image acquired by an experiment. Assuming a point source, the image is calculated as follows. The point source provides a simple light field in the Fourier plane ($\mathbf{E} = 1$). The aberrations due to the glass cell are added to the flat phase Φ and the amplitude E is modified by the aperture. The inverse FT provides the light field $\mathbf{E}$ in the image plane. By taking the square of the absolute value we get the point spread function (PSF) [Hec90], the image

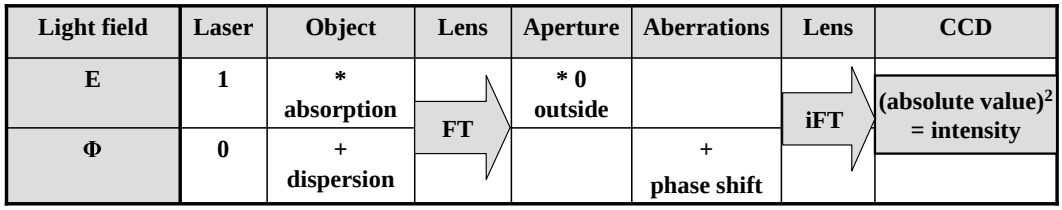

Figure 4.10.: The block diagram illustrates a computer program used to generate the image of a finite size object that can be compared to experimental data. Modifications in E are multiplied, shifts in ϕ are added to the light field. The initial light field of the laser is modified by an object. A pinhole affects only the amplitude. The FT provides the light field in the Fourier plane that is modified due to the aberrations and the aperture. The absolute square of the result of the inverse FT gives the image of the pinhole that can be compared to an image acquired in the test setup.

of the point source which is an Airy function in this case. But since we use objects of finite size (pinholes) in the test setup the calculation has to be extended. The scheme is shown in Fig. 4.10.

Fig. 4.11 a) and b) show the calculated and the measured images of a 5 μm pinhole without and with the glass plate. The agreement between theory and experiment strongly supports our calculations. In the image plane in Fig. 4.11 b), the light is spread over a wide area. However, such a wide spread of light was never observed in images of an atom cloud. The question, if we overestimate the aberrations, arises but is negated through the next excursion.

Excursion 5 *'The smaller the object, the more the light is spread out in its image.' This counter intuitive statement becomes clear when going through the diagram of Fig. 4.10 for various objects. Smaller objects have a wider spectrum in the Fourier plane. Mainly the light close to the edge of the aperture is affected by aberrations. In other words: For bigger objects the first order is not diffracted as much (see Fig. 4.12). So, the light does not experience as strong phase shifts because the aberrations are strongest towards the edge of the aperture.*

Experiments as well as theory show stronger effects of aberration for smaller objects as can be seen from the square, red points and the dashed, red curve in Fig. 4.14.

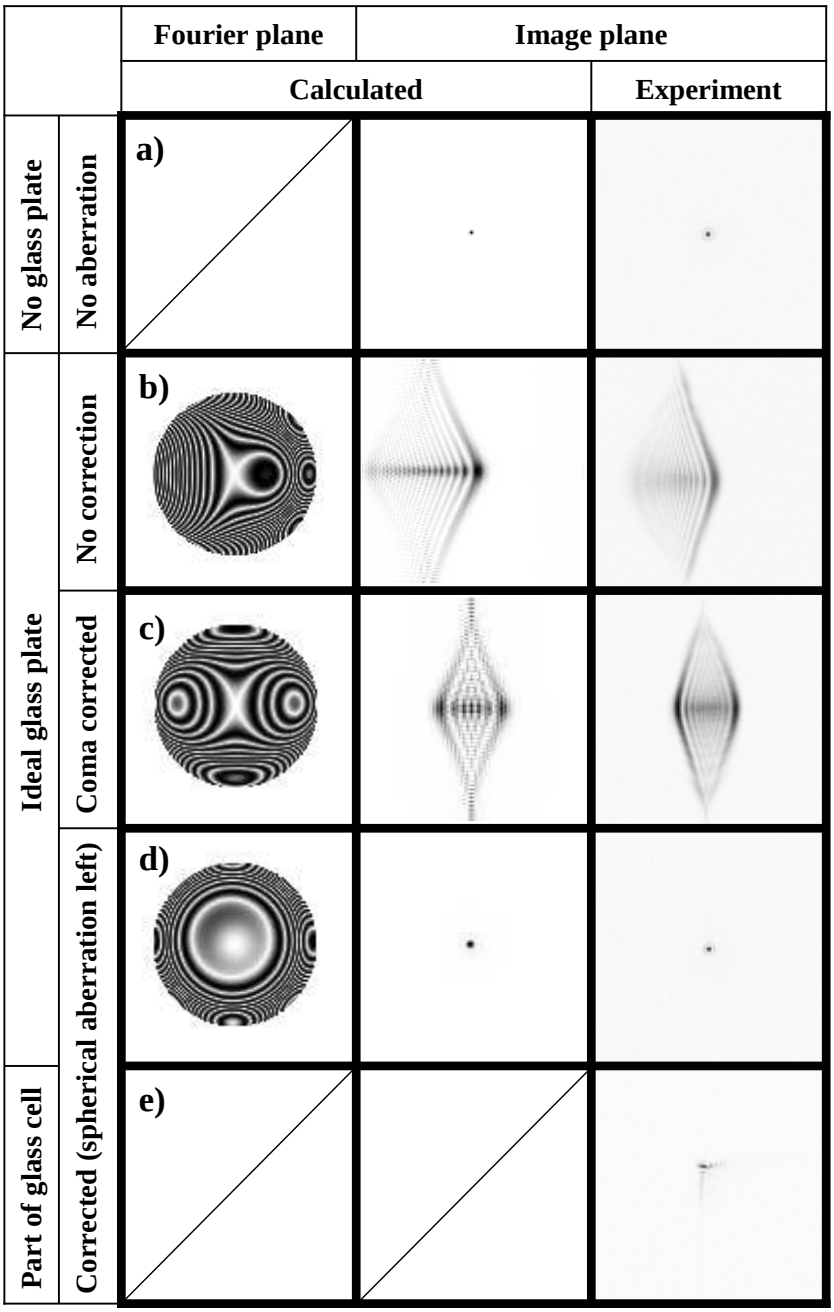

Figure 4.11.: Calculated wavefronts and images are compared to images from the test setup. The object is a 5 μm pinhole. a) shows the diffraction limited imaging system. The wavefront is simply flat. In b) through d) a glass plate with negligible surface roughness serves as 'ideal glass plate' to simulate the glass cell. The image in e) is obtained by using a piece of a broken glass cell. It cannot be simulated due to the randomness of the aberrations. The wavefront is plotted using contour lines with a spacing of λ. The images correspond to 80 μm×80 μm in the object plane

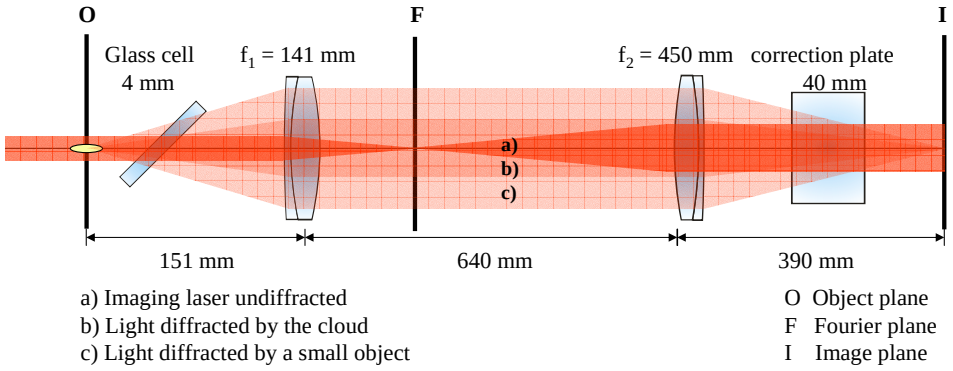

Figure 4.12.: The imaging system with glass cell and correction plate. The light distributions represent the undiffracted light of the laser and the diffracted light of two objects with different sizes. Note that the object distance is not exactly the focal length of the first lens. That is why the magnification is not 450/145 but 3.2.

Compensation of the aberrations

After having successfully quantified and identified the aberrations, we know how to compensate them. For the correction we go step by step through the Zernike coefficients. For the coefficients with the numbers 6, 4 and 8 we use the common terminology: coma, astigmatism and spherical aberration, respectively.

- **Coma** is a first order field aberration. That means that it is proportional to the distance of the image to a specific symmetry axis which is perpendicular to the image plane. Since the field in our system is very small, we can neglect coma as soon as there is no offset of coma. This is the case when the specific axis of coma coincides with the optical axis of the system. This is achieved by decentering the first lens with respect to the optical axis of the imaging beam. Without coma, the wavefront and the image are symmetric with respect to two axes, as can be seen in Fig. 4.11 c) because of the symmetry of the remaining Zernike polynomials number 4 and 8. This symmetry is used to adjust the right decentering of the lens in the experiment. Fig. 4.11 c) shows the aberrations left.

- **Astigmatism** is normally compensated with cylindrical lenses. The wavefront curvature of 7.1 wavelengths at the edge of the aperture corresponds to a focal length of about 20 m. Those cylindrical lenses are neither available nor adjustable. An alternative idea is to add an additional but perpendicular astigmatism resulting in a spherical phase shift. The spherical wavefront curvature is compensated by refocusing. Fig. 4.13 illustrates this principle. The additional astigmatism could be generated by a second glass plate before the first lens. However, this is not possible due to lack of space. Inserting it behind the second

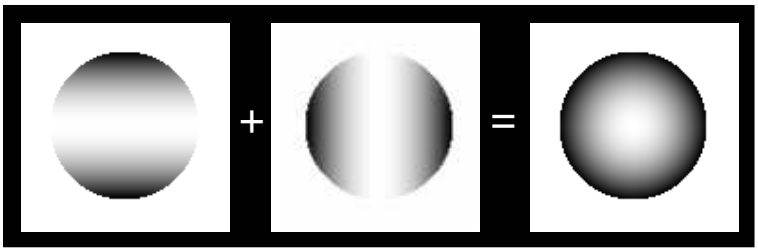

Figure 4.13.: Plotted are the wavefronts of astigmatisms that are perpendicular to each other. They add up to a spherical wavefront.

lens, as shown in Fig. 4.12, has to account for a different divergence of the light. According to [Wya92] the astigmatism is proportional to the thickness of the glass plate and proportional to the square of the divergence. The change in divergence is inverse to the magnification. Thus, a 40 mm thick glass cube, which has the same angle relative to the optical axis as the first glass plate, gives the right correction. Varying its angle to the optical axis serves as fine adjustment. The quality of this approach is shown in Fig. 4.11 d).

- **Spherical aberration** could be compensated by replacing one of the lenses by a special lens doublet. But tests, as plotted in Fig. 4.11 e), have shown that random aberrations, induced by the roughness of the glass cell, are stronger than the spherical aberration, as shown in Fig. 4.11 d). From the image in Fig. 4.11 e), one can infer the surface roughness of the glass cell which is in agreement with its specifications. Thus, we do not correct the spherical aberration because this would not significantly improve the performance of the system.

4.2.3. Performance of the imaging system

In Sec. 4.2.1 we started to design a diffraction limited imaging system where we have turned our attention to the resolving power and the signal-to-noise ratio. This discussion did not include aberrations. Our corrected imaging system is still affected by aberrations. In the following, we will find parameters to describe the performance of the imaging system.

Smaller aberrations, as shown in Fig. 4.11 d), cause a spread of light without affecting the resolving power. The Rayleigh criterion is still applicable for the resolving power but the image quality is reduced in terms of the signal-to-noise ratio. Since the spread of light reduces the signal in the zeroth order of the diffraction pattern we take the

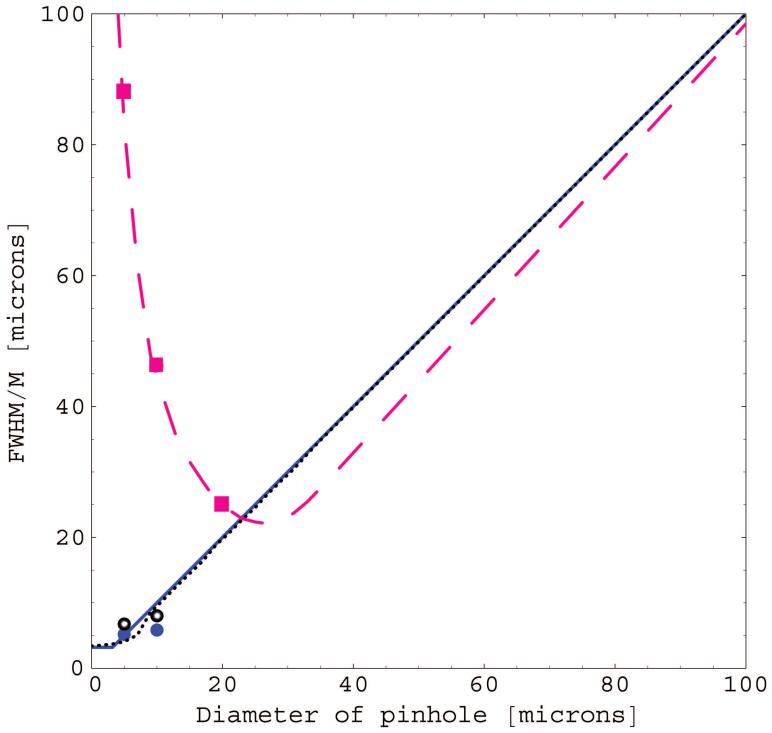

Figure 4.14.: For different pinholes, a Gaussian profile is fitted to the image. The FWHM divided by the magnification is plotted versus the pinhole diameter. The dashed, red curve shows the behavior of the uncorrected system. The image becomes bigger for smaller objects - up to 110 μm - as explained in excursion 5. The ideal curve (continuous, blue) goes down to the diffraction limit. This limit is almost reached by the corrected system (dotted, black curve) not including random aberrations. The points show experimental data. Due to wrong focusing they can become smaller than theory predicts because the minima of diffraction are arranged such that the image gets smaller. The blue point at 5 μm is derived from the image in Fig. 4.11 a), the red square from b) and the black circle from d). Fitting a Gaussian intensity profile is not adequate for larger objects. It leads to an underestimate for images with aberrations, explaining why the dashed, red curve comes below the continuous, blue curve.

Table 4.5.: We take the minima of the points in Fig. 4.14 to get a measure of the minimum resolvable distance, characterizing the resolving power. The percentage of light on an area as big as the zeroth order of the Airy function (84 % for the diffraction limited system) of the image of a 5 μm pinhole serves as a measure of the signal-to-noise ratio. The performance is given for four cases that correspond to Fig. 4.11 a), b), d) and e), respectively. 'cor.' stands for corrected.

	no plate	ideal plate	ideal plate (cor.)	glass cell (cor.)
Minimum FWHM	5.5 μm	20 μm	6 μm	9 μm
Signal in 0. order	85 %	7 %	60 %	40 %

percentage of light within the zeroth maximum as a measure of image quality. In Tab. 4.5, we show the results for different cases.

More severe aberrations can lead to images as shown in Fig. 4.11 b). The position of the minima do not correspond to the resolving power at all. Here, the full width at half maximum (FWHM) of a fitted Gaussian profile serves as a measure for the image quality. It is not directly the minimum resolvable distance because it includes the size of the object. We summarize the minimum FWHM of Fig. 4.14 in Tab. 4.5.

The performance of the imaging system in our machine is believed to be in between the test results obtained from the ideal glass plate and a piece of a broken glass cell. The resolving power is estimated to be 7 μm, limited to 8 μm by the magnification and the pixel size of the CCD camera.

All the values are derived from artificial objects. When imaging an elongated cloud one has to keep in mind that only a part of the cloud is in the focal plane. The tips of the cloud are about ± 50 μm out of focus. A simple geometric consideration yields that an infinitely small object at one of the tips appears to be as big as 12 μm. This is not a strict limit for the resolving power as this light might just cause blurring.

5. Customized Potentials for various Experiments

The ability to scan the position of the trapping beam in the x-y-plane and to image along the z-axis makes possible a variety of experiments. In this chapter, we focus on how to create different trapping potentials that can be used for various experiments. The underlying physics, explored by those experiments, is extremely rich. It will serve as motivation but a detailed discussion is beyond the scope of this thesis.

We summarize the specifications of the scanning system. It is capable of forming any potential in the x-y-plane within the following limits.

- The smallest extension and the steepest edge of the potential are given by the trapping beam itself which has a Gaussian beam profile with a waist of $w_3 = 54\ \mu$m.
- The size of the largest pattern is limited by the largest translation $D_3 = 400\ \mu$m.
- The modulation of translation cannot be faster than the bandwidth $BW = 950$ kHz.

A modulation with frequency ω can affect the atoms in the trap with radial trap frequency $\omega_\perp$ in three different ways.

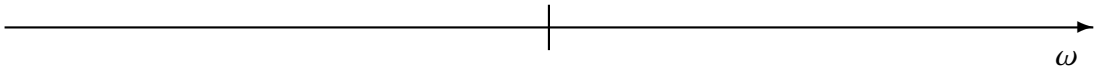

$\omega \ll \omega_\perp$ $\approx 2\pi \times 10$ Hz	$\omega_\perp$ $\approx 2\pi \times 400$ Hz	$\omega \gg \omega_\perp$ $\approx 2\pi \times 40,000$ Hz
The position of the potential changes adiabatically. The atom cloud follows and does not show any heating effects.	The modulation is on resonance with a mode in the trap. This can be used for driving collective excitations. Noise on this frequency leads to heating.	The atoms cannot follow on this timescale. The modulation leads to a time-averaged potential. No heating is observed for $\omega > 100 \times \omega_\perp$.

With the bandwidth as given above, all three regimes are accessible. Fig. 5.1 shows the potentials that we will discuss in the following sections.

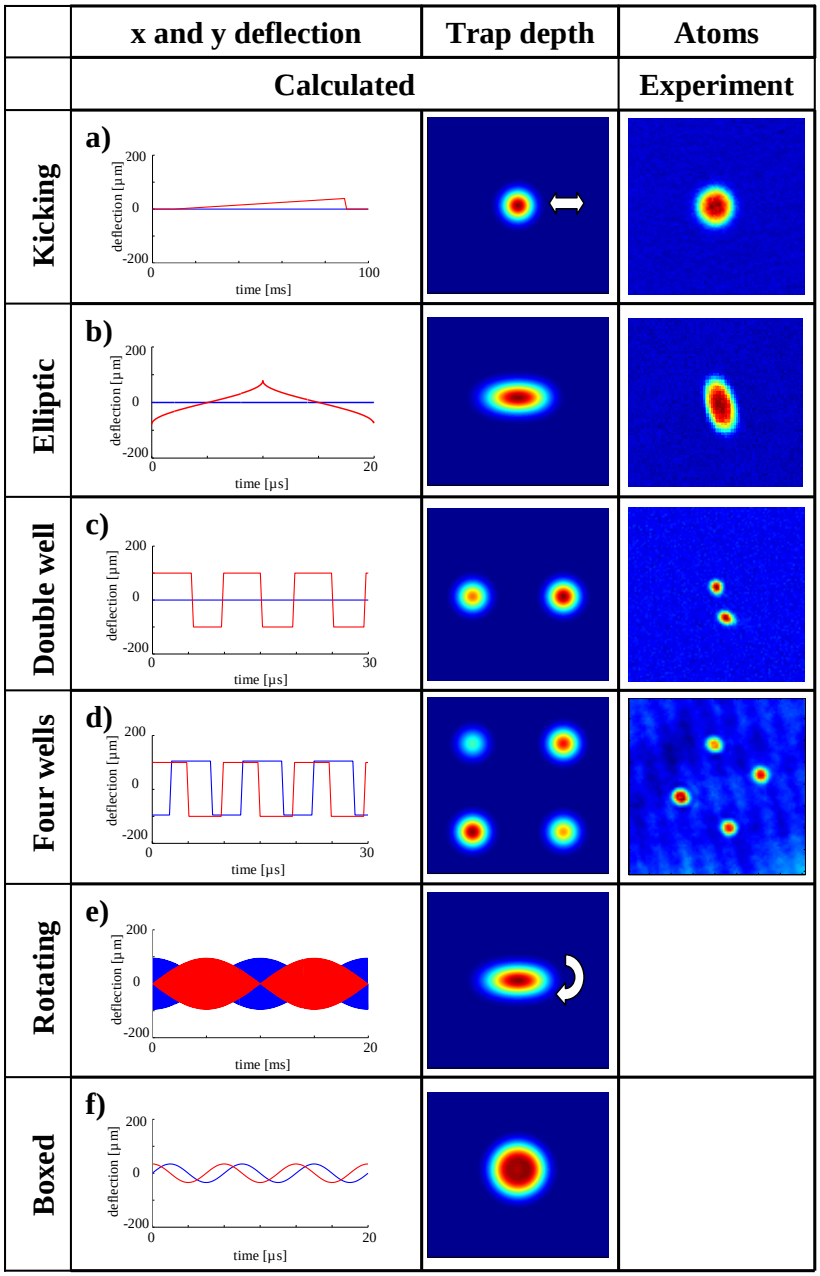

Figure 5.1.: For various modulation schemes, the translations versus time $x_D(t)$ (light, red curve) and $y_D(t)$ (dark, blue curve), the calculated potential depth and - when available - a TOF image of the atom cloud are plotted. In the actual experiments, the amplitude of translation is optimized as mentioned in the text. Note the difference in timescales of experiments in a), e) where the cloud follows the variation of potential compared to the experiments b), c), d), f) where we create time-averaged potentials. The size of the plots of potential depth and the images is 400 μm×400 μm. The calculated potentials are plotted with respect to the deflection axes of the AOMs and the images are relative to the axes of the CCD camera which explains the different angles.

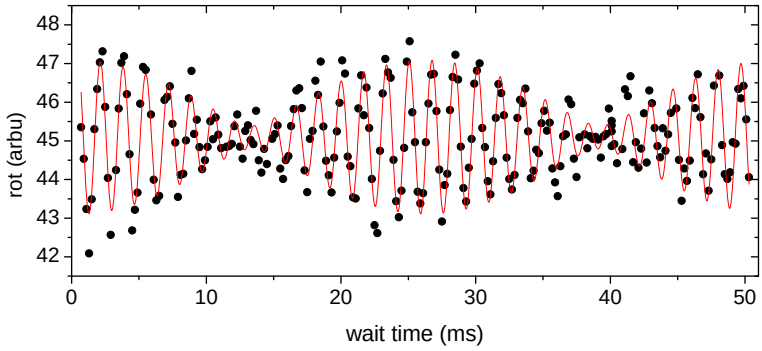

Figure 5.2.: Oscillation along the axis *rot* versus waiting time after excitation. The pronounced beating suggests that the principal axes have angles $\sim \pm 45°$ relative to *rot*.

5.1. Displacing the trap: Trap frequency measurement

Here, we describe a change in potential that is used to determine the radial trap frequency $\omega_\perp$. This crucial parameter enters the calculation of the Fermi energy and is especially important for measurements on collective excitations because the frequencies of the modes must be normalized to $\omega_\perp$.

It is possible to derive the trap frequency from the beam parameters and the beam power, but it is much more direct and precise to measure the center-of-mass oscillation of the trapped atom cloud. To excite such a sloshing mode, we dislocate the cloud along one axis adiabatically. Then, the potential is instantaneously snapped back to its original position initializing the sloshing mode. The timing is plotted in Fig. 5.1 a) where the amplitude of displacement is not to scale. As a trade-off between high sloshing amplitude and low anharmonicity, the amplitude is chosen such that the potential energy is about 10 % of the trap depth.

The trap is not perfectly cylindrically symmetric because of the slightly elliptic beam profile of the laser beam and further imperfections in our optical setup. The following excursion describes an algorithm to derive the two trap frequencies $\omega_{x'}$ and $\omega_{y'}$ along the two principal axes x' and y' from one set of measurements. It is more common to describe the potential in terms of the radial trap frequency $\omega_\perp = \sqrt{\omega_{x'}\omega_{y'}}$ and ellipticity $\epsilon = (\omega_{x'} - \omega_{y'})/\omega_\perp$. The uncertainty in $\omega_\perp$ is less than 0.5 %. This method is crucial for the precision of measurements of collective excitations in the crossover regime. Breathing modes probe the compressibility and this can be compared to the compressibility derived from a theoretically predicted equation of state. Our precise measurements allow for the distinction of different theoretical approaches [Alt07, Alta].

Excursion 6 *Sloshing of the atom cloud along one of the principal axes (x' or y') would show up as a slowly damped harmonic oscillation providing only one frequency.*

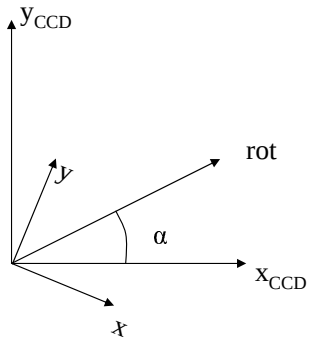

Figure 5.3.: Images provide the position of the cloud with respect to the camera axes x_{CCD} and y_{CCD}. For the algorithm, we introduce the axis *rot* that has an angle α relative to x_{CCD}. Scanning with one of the AOMs provides an initial dislocation in x- or y-direction. The orientation of the principal axes x' and y' of ellipticity are not of interest.

Exciting both axes simultaneously and with the same amplitude leads to a well pronounced beating as shown in Fig. 5.2. By just exciting with one AOM (along x or y) we do not achieve the same amplitudes in general and the beating signal is less pronounced. Still, we can extract the two frequencies using the following algorithm: The two coordinates x_{CCD} and y_{CCD} of the position of the cloud on the camera are translated into a projection onto the axis rot. This axis has an angle α relative to x_{CCD} as illustrated in Fig. 5.3. For various α, a damped oscillation is fitted to the oscillation along rot. We find two values for α with minimal damping. There, rot is supposed to coincide with one of the principal axes. The fitted frequencies for those angles are the trap frequencies.

5.2. Elliptic potential: Exciting quadrupole modes

As above, we use the scanning system to excite a mode of the atom cloud. A change in potential is adiabatically ramped up and suddenly switched back, leaving the cloud with potential energy that leads to an oscillation. To excite a quadrupole mode, we do not move the potential but change its shape. This is achieved by a time-averaged potential.

To excite a quadrupole mode, the cylindrically symmetric trapping potential (here, the ellipticity of the beam is neglected) is changed to a potential that is elliptic in the x-y-plane and harmonic along both principal axes. Following the recipe for calculating time-averaged potentials in excursion 7, one can show that this is achieved by a periodic modulation with a function as plotted in Fig. 5.1 b). A full domain of an arcsin function is repeated with alternating sign. Note the different timescale compared to Fig. 5.1 a). To excite the pure surface mode, an excitation of a compression mode has to be avoided by regulating the trap depth, i.e. the power of the laser beam. Since the

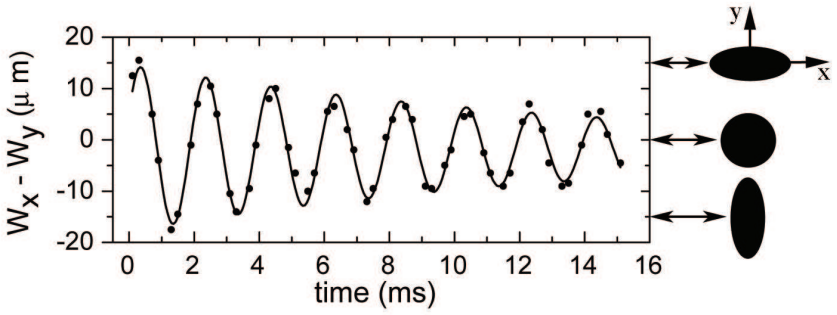

Figure 5.4.: The difference of the width of the cloud in x- and y-direction versus oscillation time of a typical quadrupole mode in the hydrodynamic regime. The cloud oscillates as sketched on the right hand side.

unperturbed surface mode is an oscillation without compression, its frequency does not depend on the equation of state. It is used to probe the transition from the hydrodynamic to the collisionless regime [Coz03]. A typical oscillation in the hydrodynamic regime is shown in Fig. 5.4. In the collisionless regime the aspect ratio does not invert. The cloud oscillates from elliptic to round [Altb].

Excursion 7 *The time-averaged trap potential $U(x, y)$ is calculated from the functions $x_D(t)$, $y_D(t)$ which give the position x and y of the trapping beam at time t. As long as the time-averaged potential is not generated by a stochastic translation, the functions $x_D(t)$ and $y_D(t)$ are periodic and have a least common period P which has to be smaller than $2\pi/(100 \times \omega_\perp)$ in order to avoid heating. The time-averaged potential is proportional to the original trap depth U_0 at $x = y = 0$ and reads*

$$U(x,y) = \frac{U_0}{P} \int_0^P dt\, e^{-\left((x_D(t)-x)^2+(y_D(t)-y)^2\right)/w_3^2}. \tag{5.1}$$

5.3. Double well potential: Interference experiment

We use the scanning system to split the atom cloud into two wells.

A double well potential is created by modulating the AOMs with a square function as shown in Fig. 5.1 c). In practice, one of the two wells is always deeper at the beginning of the ramp and most of the atoms fall into this well. To achieve equal distribution, the duty cycle of the square function is adjusted.

One motivation for the splitting of the cloud are interference experiments. Interference is a consequence of long-range phase coherence and serves as an indirect proof of superfluidity [And98, Shi04]. Mapping out the superfluidity of a Fermi gas is very interesting in the crossover regime where the scattering length is high, i.e. the interaction is strong. However, this strong interaction destroys the phase coherence during

expansion before the two clouds overlap. One possibility is to very quickly ramp the magnetic field to a field strength where the scattering length is low [Chi06]. By now, our setup does not permit that.

5.4. Four wells

A four well potential, as plotted in Fig. 5.1 d), is an extension of the double well potential. The starting point is a double well formed by the modulation of one AOM. Ramping up a square modulation, that is about 90° out of phase, on the other AOM repeats the splitting. Again, the atoms prefer the well that is slightly deeper. To accomplish equal splitting of both clouds two parameters have to be optimized: The phase and the duty cycle of the modulation of the other AOM.

5.5. Rotating elliptic potential: Scissors mode and rotation

In this section, we introduce a rotating elliptic potential for future experiments. It is generated by modulating the AOMs on two different timescales. The fast modulation provides an elliptic time-averaged potential and the slow modulation provides a rotation of this ellipse which is adiabatic. According to [Coz03] such a potential can be used to distinguish whether the atom cloud is superfluid or normally hydrodynamic.

To excite a scissors mode, the initial potential is elliptic, as it is for the excitation of a quadrupole mode. Then, the axis of the ellipse is tilted in the x-y-plane. The oscillation around the new equilibrium position is called scissors mode. Neither the surface nor the volume of the cloud changes. Thus, this mode is independent of the equation of state and is suitable to investigate if the system is hydrodynamic or collisionless.

The previous experiments with quadrupole or scissors modes proof the hydrodynamic behavior but do not distinguish between the superfluid and the normally hydrodynamic regime. The following experiment takes advantage of the irrotationability of a superfluid to discern it from a rotating Fermi gas in the collisional regime. The starting condition is a rotating elliptic trap as plotted in 5.1 e) and then the rotation is stopped. For the superfluid a scissors mode is excited due to initial kinetic energy, whereas, before, it was due to the initial potential energy. The Fermi gas shows a different oscillation because of the induced rotational flow [Coz03]. The rotation has to be low enough not to excite vortices in the superfluid. Vortices can also be used to make this distinction. But measurements of collective oscillation promise more quantitative and precise results for the position of the phase transition.

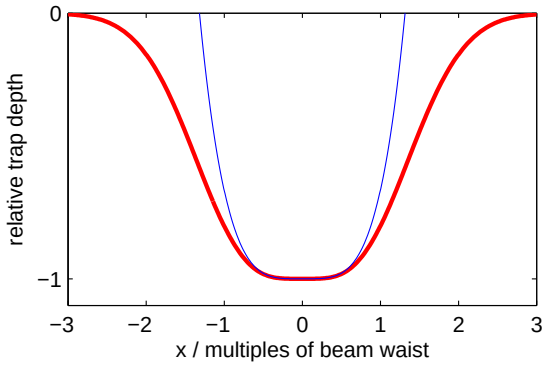

Figure 5.5.: Relative trap depth along the x-axis (thick, red curve). The modulation is according to the scheme in Fig. 5.1 f). For a peak-to-peak modulation amplitude of $w_3/\sqrt{2}$ the quadratic term vanishes at the origin. The thin, blue curve represents the quartic term which fits only the very bottom of the trap.

5.6. Quartic and box-like potentials: Fast rotation and homogeneous system

The scanning system can be used to create potentials that are optimized for specific experiments. As an example we take a potential that is flat on the bottom. This can only be true for a finite volume because the atoms have to be trapped. Where the potential is flat, the chemical potential of the atom cloud is constant. Such a system is an approximation of a homogeneous system, which is often treated in theories on ultracold Fermi gases.

To discuss non-harmonic potentials, we write down the Taylor expansion of a symmetric trap in one dimension:

$$U(x) - U(0) \sim \sum_{i \in 2\mathbb{N}} \frac{1}{i!} k_i x^i \tag{5.2}$$

The expansion coefficient k_2 gives the harmonic confinement and k_4 gives the quartic confinement; higher terms are neglected. The Gaussian beam profile is approximated by a slightly negative k_4.

Moving the beam along a small cycle around the center position reduces the confinement on the bottom of the trap. This reduces the trap frequency, derived from k_2, and provides a positive k_4 accounting for the steep outer part of the potential. Such a quartic potential can be used for experiments with fast rotation where the rotation frequency is higher than the trap frequency [Bre04]. For a specific radius of the cycle, the quadratic term vanishes, as plotted in Fig 5.5. This is a simple way to create a box-like potential as shown in 5.1 f). The atoms experience a homogeneous potential on the bottom of the trap. In an ideal box potential only k_∞ does not vanish. It is not

trivial to make higher coefficients vanish in two dimensions. Sophisticated scanning schemes have to be developed. One possibility is to implement a generic algorithm. This discussion did not consider the potential along the z-axis where we cannot achieve a box-like confinement with the scanning system alone.

6. Conclusion and Outlook

Ultracold fermionic gases offer intriguing new possibilities to investigate the BEC-BCS crossover. In this thesis we presented two experimental upgrades for control and detection which are currently used to extend this exploration.

In our experiment, an elongated cloud of ultracold ^{6}Li atoms is prepared in an optical dipole trap formed by a focused laser beam [Joc04, Bar05]. We designed and implemented a scanning system using AOMs to deflect this trapping beam. A change in the radio frequency of one of the AOMs results in a displacement of the trap. If this change is on a timescale much smaller than the trap frequency $\omega_\perp$, the atoms follow the trap adiabatically. If it is fast compared to $\omega_\perp$, the atoms are in a non-equilibrium position of the displaced trap which leads to an oscillation around the new equilibrium. The scanning system can also be used to change the shape of the trapping potential. A modulation of the deflection, far above $\omega_\perp$, leads to time-averaged potentials because the atoms just follow the gradient of the average laser intensity. Besides this enhancement of control of the sample, we also set up a new imaging system to detect the radial column density of the cloud. Since the optical axis is not normal to the window of the vacuum chamber, the window induced aberration. We demonstrated that these aberrations could be compensated by an additional tilted glass plate; this improvement led to high resolving power.

After having discussed the implementation of our upgrades, we presented various deflection schemes for the scanning system. The schemes provided customized potentials for various experiments which were outlined in this thesis.

- Some of these potentials have already been used to study collective excitations in the BEC-BCS crossover [Alta]. As an example, we described a procedure to very precisely determine $\omega_\perp$. This precision was crucial for the measurement of the frequency of breathing mode normalized to $\omega_\perp$. The results allowed for a test of theoretical models of the equation of state in the BEC-BCS crossover [Alt07].

- Other potentials will be used in future experiments. As an example, we presented the realization of a rotating elliptic potential. This can be used to observe the transition from a superfluid to a normally hydrodynamic regime [Coz03].

- We also explained how to create non-harmonic potentials. E.g. box-like potentials may be used to confine systems which are nearly homogeneous. Such sys-

tems will be suited for radio-frequency measurements of the pairing gap [Chi04] because the line shapes are expected to be easier to interpret. Phase separation [Zwi06, Par06] may also be interesting to study in a homogeneous system.

We are currently establishing a variety of methods, which are based on the scanning system, to diagnose different properties of the atom cloud. The ability to control the confinement of the atom cloud will be used in various future experiments, making the scanning system a universal tool.

We look forward to facing future experimental challenges, and we are open to surprising results.

A. Appendix

A.1. Detection of particle number by absorption imaging

The number of particles N in a cloud of ultracold atoms is a crucial parameter. Important quantities, e.g. the Fermi energy, depend on it and many measurements are based on losses that are derived from a change in N. Most prominently, N is measured by detecting scattered laser light with a photodiode. In the following, we discuss how to infer N from absorption imaging.

The decrease in laser intensity $I(\mathbf{x})$ at the position $\mathbf{x} = (x, y, z)$ along the axis of the imaging beam (z) is given by

$$\frac{dI(\mathbf{x})}{dz} = -\hbar\omega\gamma\eta(\mathbf{x}) \tag{A.1}$$

where ω is the laser frequency, $\eta(\mathbf{x})$ the density of atoms and the total scattering rate γ is given by

$$\gamma = \frac{\frac{I}{I_s}\frac{\Gamma}{2}}{1 + \frac{I}{I_s} + (\frac{2\delta}{\Gamma})^2} \tag{A.2}$$

where Γ is the natural line width, δ the detuning and I_s the saturation intensity as discussed in more detail in textbooks [Met99].

For small saturation parameter $S = I/I_s$ and no detuning, the denominator in Eq. A.2 is approximately one. With these assumptions Eq. A.1 results in a simple differential equation. The solution is

$$\frac{I(x, y)}{I_0(x, y)} = \exp\left(-\sigma \int dz\, \eta(\mathbf{x})\right), \tag{A.3}$$

where we have introduced the scattering cross section $\sigma = \hbar\omega\Gamma/(2I_s)$ and $I_0(x, y)$ is the initial laser intensity. As we measure I/I_0 in our experiment, we get the integral $\int dz\ \eta(\mathbf{x})$, called column density. The particle number is gained by integrating the column density over x and y.

$$N = \int dxdy \frac{ln\frac{I_0(x,y)}{I(x,y)}}{\sigma} \tag{A.4}$$

In our experiment, this method does not provide the same result as fluorescence detection. It is off by a factor of four. The assumption of a small saturation parameter is not valid and two additional effects have to be taken into account: The orientation of the quantization axis of the atoms relative to the imaging beam and the change in detuning because of recoil events.

Intensity not much smaller than saturation intensity

When the saturation parameter S is not small Eq. A.1 has to be solved with the full expression for γ resulting in the column density:

$$\int dz\, \eta(\mathbf{x}) = \frac{1}{\sigma}\left(A\, ln\frac{I}{I_s} - A\, ln\frac{I_0}{I_s} + \frac{I}{I_s} - \frac{I_0}{I_s}\right), \tag{A.5}$$

where we have introduced $A = 1 + \left(\frac{2\delta}{\Gamma}\right)^2$.

Quantization axis different from beam axis

The signal is improved when each atom scatters more than one photon. Therefore, the imaging laser is tuned to the closed transition. As we image in strong magnetic fields in the Paschen-Back regime, one such transition is found from either of the two lowest $2S_{1/2}$ states with $m_j = -1/2$ to $2P_{3/2}$ with $m_j = -3/2$. This is a σ_- transition with respect to the quantization axis that is forced by the magnetic field axis. In our machine, the propagation and polarization axis of the linearly polarized imaging beam are perpendicular to the quantization axis. This is a special case of the derivation in [Geh03] where the incident light is decomposed into a polarization component that couples to the σ_- transition and one that does not and where the dipole pattern of the excitation is taken into account. It is found that half of the light drives the transition. This is implemented by the substitution

$$I_s \rightarrow I_s' = 2I_s. \tag{A.6}$$

This substitution also enters the cross section.

Recoil induced detuning

Every time an atom absorbs and spontaneously emits a photon into a random direction it takes over, on average, the momentum of the incoming photon. From this, the Doppler shift leads to a detuning δ_{recoil}. For the very light ^{6}Li $\delta_{recoil} = 0.15$ MHz, δ_{recoil} is small compared to the power-broadened linewidth $\Gamma' = \sqrt{1+S}\Gamma$ which is about $\sqrt{2}$ 6 MHz. But since an atom is pushed about ten times during an imaging laser pulse of duration t, the effect is not negligible. It will be taken into account by replacing γ in Eq. A.5 by an effective scattering rate γ'. Say γ' is simply the mean number of recoil

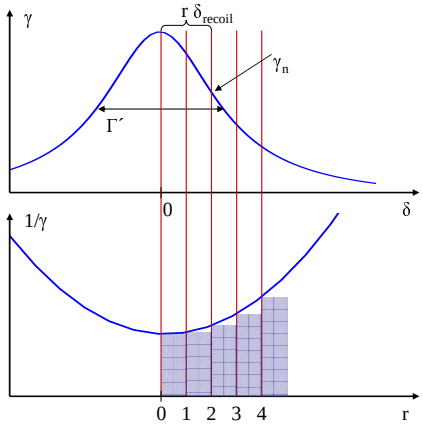

Figure A.1.: The plot of scattering rate versus detuning shows that γ changes after each recoil event. The mean duration of each event is given by the reciprocal scattering rate. Thus, the sum, as illustrated by the shaded region, is the time r events take. For calculating the average number of events R from the laser pulse duration t, the sum is approximated by an integral.

events R during the laser pulse over t. Thus we shift the problem of calculating γ' to the calculation of R.

We define the scattering rate after the r^{th} recoil event γ_r as plotted in the upper graph of Fig. A.1. γ_r is given by Eq. A.2 when inserting $r\delta_{recoil}$ for δ. The time that elapses, on average, between two scattering events is $1/\gamma_r$. The total time of R events is a sum as plotted in the lower graph of Fig. A.1 but when approximated by an integral one can calculate the average noninteger number of events R during the laser pulse by solving

$$\int_0^R dn\ \frac{1}{\gamma_r} = t. \tag{A.7}$$

And the effective scattering rate is $\gamma' = R/t$. For ^{6}Li and $S = 1$ it is about 4 % smaller than γ. This correction is implemented by multiplying the right side of equation A.5 with γ/γ'.

The final equation is

$$\int dz\ \eta(z) = \frac{\gamma}{\gamma'}\frac{2}{\sigma}\left(A\ ln\frac{I}{I'_s} - A\ ln\frac{I_0}{I'_s} + \frac{I}{I'_s} - \frac{I_0}{I'_s}\right) \tag{A.8}$$

where I'_s also enters σ. Using this equation to evaluate absorption images, the particle number agrees with the one derived from fluorescence detection. In contrast to Eq. A.1 one needs the intensity I from the image with atoms and I_0 from the division image separately to evaluate Eq. A.8.

A.2. Fast shutter for the imaging system

Since we image along the trapping beam the camera is on its axis. Even two dichroic mirrors can't extinct all the light. *In situ* images show the remaining trap light. To get undisturbed time of flight images nearly after release a very fast shutter is implemented.

We use the quick head armature of a standard computer hard drive. It is weight reduced and an aluminum foil is glued on for covering a large area. The coil in the head actuator is driven by the electronics shown in Fig. A.2. When the TTL opens the gate, the capacitor provides some current at full voltage. This is used for fast acceleration. Then low voltage holds the shutter in open position. The electronics is only good for opening and takes some time for charging. The shutter is closed by a spring. Tab. A.1 summarizes the features.

The speed allows for a shot less than 0.5 ms after release. This is about 5 times better than for commercial shutters.

Table A.1.: Performance of the shutter. The speed and reproducibility are measured at the position where the shutter crosses the optical axis. The charging time is the least time between two shots. The screened area is the field that the shutter can cover.

Speed	9.1 m/s
Reproducibility	1.7 μs
Charging time	0.5 s
Screened area	$(20\ \text{mm})^2$

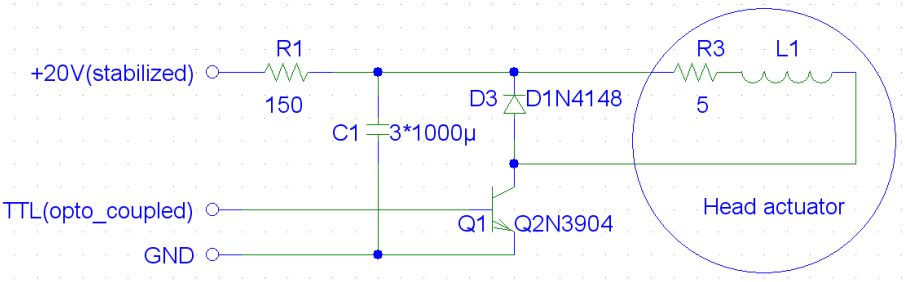

Figure A.2.: Circuit diagram for the electronics driving the shutter

B. Thanks

Writing this thesis reminds me of what I've learned and of all the discussions I've had during the last year. Thus, I would like to thank all the members of our group who shared their knowledge and their enthusiasm with me. The friendly atmosphere never made me stop asking questions. So, I'm especially grateful to my lab mates Matthew Wright, Alexander Altmeyer and Stefan Riedl for their patience when explaining.

Learning how to work in a laboratory is just one facet of expertise a scientist should have. To see what is going on at the frontier of physics and what the necessary steps are to push physics further is another. I think there is no better place to learn both than in such a distinguished group. Thanks, Johannes Hecker-Denschlag and Rudi Grimm[1] for letting me be part of your group.

The experience, not just to learn but also to contribute to physics, showed me again that this is the field I want to work in. Also my brothers and sisters have found fields that suit their skills and demands; but different ones. That shows me how much my siblings and I have profit from our upbringing. That's why I want to thank my parents for much more than just for their support during my studies.

Physics is the field that comprises many qualities I appreciate: Logic, electronics, mechanics, teamwork and more. That makes it fulfilling and a major part of your life. You focus; impulses from outside are needed to show you what got out of your field of view. To climb the mountains around Innsbruck might have been one way to get a glimpse of what's beyond the horizon but the true perspective came from my friends. Thanks.

[1] That is what I wrote before I handed this thesis to Rudi Grimm for proof-reading. After long discussions and after many cycles of rewriting, I have learned that there is one more facet of expertise that I will have to learn: Writing. Special thanks for this lesson.

References

[Alta] A. Altmeyer, Ph.D. thesis, Universität Innsbruck, (in preparation).

[Altb] A. Altmeyer, S. Riedl, C. Kohstall, M. J. Wright, J. H. Denschlag, and R. Grimm, *Collective Oscillations of the radial quadrupole mode in the BEC-BCS crossover* (in preparation).

[Alt07] A. Altmeyer, S. Riedl, C. Kohstall, M. Wright, R. Geursen, M. Bartenstein, C. Chin, J. H. Denschlag, and R. Grimm, *Precision Measurements of Collective Oscillations in the BEC-BCS Crossover*, Phys. Rev. Lett. **98**, 040401 (2007).

[And95] M. H. Anderson, J. R. Ensher, M. R. Matthews, C. E. Wieman, and E. A. Cornell, *Observation of Bose-Einstein Condensation in a Dilute Atomic Vapor*, Science **269**, 198 (1995).

[And98] B. P. Anderson and M. A. Kasevich, *Macroscopic Quantum Interference from Atomic Tunnel Arrays*, Science **282**, 1686 (1998).

[Bar57] J. Bardeen, L. N. Cooper, and J. R. Schrieffer, *Theory of Superconductivity*, Phys. Rev. **108**, 1175 (1957).

[Bar05] M. Bartenstein, *From Molecules to Cooper Pairs: Experiments in the BEC-BCS Crossover*, Ph.D. thesis, Universität Innsbruck (2005).

[Bre04] V. Bretin, S. Stock, Y. Seurin, and J. Dalibard, *Fast rotation of an ultra-cold Bose gas*, Phys. Rev. Lett. **92**, 050403 (2004).

[Chi04] C. Chin, M. Bartenstein, A. Altmeyer, S. Riedl, S. Jochim, J. Hecker Denschlag, and R. Grimm, *Observation of the pairing gap in a strongly interacting Fermi gas*, Science **305**, 1128 (2004).

[Chi06] J. K. Chin, D. E. Miller, Y. Liu, C. Stan, W. Setiawan, C. Sanner, K. Xu, and W. Ketterle, *Evidence for Superfluidity of Ultracold Fermions in an Optical Lattice*, Nature **443**, 961 (2006).

[Coz03] M. Cozzini and S. Stringari, *Fermi Gases in Slowly Rotating Traps: Superfluid vs Collisional Hydrodynamics*, Phys. Rev. Lett. **91**, 070401 (2003).

[Els00] T. Elsässer, *Stehwellenfalle in einem Resonator*, diploma thesis, Max-Planck-Institut für Kernphysik, Heidelberg (2000).

[Fri00] N. Friedman, L. Khaykovich, R. Ozeri, and N. Davidson, *Compression of cold atoms to very high densities in a rotating-beam blue detuned optical trap*, Phys. Rev. A **61**, 031403 (2000).

[Geh03] M. E. Gehm, *Preparation of an Optically-Trapped Degenerate Fermi Gas of ^{6}Li: Finding the Route to Degeneracy*, Ph.D. thesis, Duke University (2003).

[Gri] R. Grimm, *Ultracold Fermi gases in the BEC-BCS crossover: a review from the Innsbruck perspective*, in: *Proceedings of the International School of Physics "Enrico Fermi" 2006*, (in preparation).

[Gri00] R. Grimm, M. Weidemuller, and Y. B. Ovchinnikov, *Optical dipole traps for neutral atoms*, Adv. At. Mol. Opt. Phys. **42**, 95 (2000).

[Hec90] E. Hecht, *Optics*, Addison-Wesley Publishing Company, 1990.

[Hen03] G. Hendel, *Atom - Atom Wechselwirkung in einem ultrakalten, fermionischen Gas*, diploma thesis, Universität Innsbruck (2003).

[Hod01] E. Hodby, G. Hechenblaikner, S. A. Hopkins, O. M. Maragò, and C. J. Foot, *Vortex Nucleation in Bose-Einstein Condensates in an Oblate, Purely Magnetic Potential*, Phys. Rev. Lett. **88**, 010405 (2001).

[Ino98] S. Inouye, M. R. Andrewa, J. Stenger, H.-J. Miesner, D. M. Stamper-Kurn, and W. Ketterle, *Observation of Feshbach resonances in a Bose-Einstein condensate*, Nature **392**, 151 (1998).

[Joc00] S. Jochim, *Aufbau einer Apparatur zum magnetooptischen Einfang von fermionischen Lithiumatomen*, diploma thesis, Max-Planck-Institut für Kernphysik, Heidelberg (2000).

[Joc03] S. Jochim, M. Bartenstein, A. Altmeyer, G. Hendl, S. Riedl, C. Chin, J. Hecker Denschlag, and R. Grimm, *Bose-Einstein Condensation of Molecules*, Science **301**, 2101 (2003).

[Joc04] S. Jochim, *Bose-Einstein Condensation of Molecules*, Ph.D. thesis, Universität Innsbruck (2004).

[Ket99] W. Ketterle, D. S. Durfee, and D. M. Stamper-Kurn, *Making, probing and understanding Bose-Einstein condensates*, in: M. Inguscio, S. Stringari, and C. E. Wieman (Eds.), *Proceedings of the International School of Physics - Enrico Fermi*, 67, IOS Press, 1999.

[Kup68] C. G. Kuper, *An Introduction to the Theory of Superconductivity*, Clarendon Press, 1968.

[Leg80] A. J. Leggett, *Diatomic Molecules and Cooper Pairs*, in: A. Pekalski and R. Przystawa (Eds.), *Modern Trends in the Theory of Condensed Matter*, 13–27, Springer-Verlag, Berlin, 1980.

[Mat99] M. R. Matthews, B. P. Anderson, P. C. Haljan, D. S. Hall, C. E. Wieman, and E. A. Cornell, *Vortices in a Bose-Einstein Condensate*, Phys. Rev. Lett. **83**, 2498 (1999).

[Men02] C. Menotti, P. Pedri, and S. Stringari, *Expansion of an Interacting Fermi Gas*, Phys. Rev. Lett. **89**, 250402 (2002).

[Met99] H. J. Metcalf and P. van der Straten, *Laser Cooling and Trapping*, Springer, 1999.

[Mil01] V. Milner, J. L. Hanssen, W. C. Campbell, and M. G. Raizen, *Optical Billiards for Atoms*, Phys. Rev. Lett. **86**, 001514 (2001).

[Mor01] H. Moritz, *Fermionisches Lithium in einer Resonatordipolfalle*, diploma thesis, Max-Planck-Institut für Kernphysik, Heidelberg (2001).

[Noz85] P. Nozières and S. Schmitt-Rink, *Bose Condensation in an Attractive Fermion Gas: From Weak to Strong Coupling Superconductivity*, J. Low Temp. Phys. **59**, 195 (1985).

[Par06] G. B. Partridge, W. Li, R. I. Kamar, Y. an Liao, and R. G. Hulet, *Pairing and Phase Separation in a Polarized Fermi Gas*, Science **311**, 503 (2006).

[Pet02] C. J. Pethick and H. Smith, *Bose-Einstein Condensation in Dilute Gases*, Cambridge University Press, 2002.

[Pit03] L. Pitaevskii and S. Stringari, *Bose-Einstein Condensation*, Oxford University Press, 2003.

[Rie04] S. Riedl, *Untersuchung stark wechselwirkender fermionischer Quantengase mittels Absorptionsabbildung*, diploma thesis, Universität Innsbruck (2004).

[Shi04] Y. Shin, M. Saba, T. A. Pasquini, W. Ketterle, D. E. Pritchard, and A. E. Leanhardt, *Atom interferometry with Bose-Einstein condensates in a double-well potential*, Phys. Rev. Lett. **92**, 050405 (2004).

[Wya92] J. C. Wyant and K. Creath, *Basic Wavefront Aberration Theory for Optical Metrology*, Applied optics and optical engineering **9** (1992).

[Zwi05] M. W. Zwierlein, J. R. Abo-Shaeer, A. Schirotzek, C. H. Schunck, and W. Ketterle, *Vortices and Superfluidity in a Strongly Interacting Fermi Gas*, Nature **435**, 1047 (2005).

[Zwi06] M. W. Zwierlein, A. Schirotzek, C. H. Schunck, and W. Ketterle, *Fermionic Superfluidity with Imbalanced Spin Populations and the Quantum Phase Transition to the Normal State*, Science **311**, 492 (2006).